Time-varying double-peaked emission lines following the sudden ignition of the dormant galactic nucleus AT2017bcc

E. J. Ridley [ID],[1,2]★ M. Nicholl [ID],[3] C. A. Ward,[4] P. K. Blanchard,[5] R. Chornock [ID],[6] M. Fraser [ID],[7]
S. Gomez,[8] S. Mattila,[9,10] S. R. Oates [ID],[1,2] G. Pratten,[1,2] J. C. Runnoe [ID],[11] P. Schmidt,[1,2]
K. D. Alexander,[12] M. Gromadzki [ID],[13] A. Lawrence [ID],[14] T. M. Reynolds [ID],[9,15,16] K. W. Smith,[3]
Ł. Wyrzykowski,[13] A. Aamer [ID],[2,3] J. P. Anderson,[17,18] S. Benetti [ID],[19] E. Berger,[20] T. de Boer,[21]
K. C. Chambers,[21] T.-W. Chen,[22] H. Gao [ID],[21] C. P. Gutiérrez [ID],[23,24] C. Inserra [ID],[25] T. Kangas [ID],[26,27]
G. Leloudas,[28] E. A. Magnier,[21] L. Makrygianni,[29] T. Moore,[3] T. E. Müller-Bravo,[23,24] S. J. Smartt [ID],[30,3]
K. V. Sokolovsky [ID],[31,32] R. Wainscoat[21] and D. R. Young[3]

Affiliations are listed at the end of the paper

ABSTRACT

We present a pan-chromatic study of AT2017bcc, a nuclear transient that was discovered in 2017 within the skymap of a reported burst-like gravitational-wave candidate, G274296. It was initially classified as a superluminous supernova, and then reclassified as a candidate tidal disruption event. Its optical light curve has since shown ongoing variability with a structure function consistent with that of an active galactic nucleus, however, earlier data show no variability for at least 10 yr prior to the outburst in 2017. The spectrum shows complex profiles in the broad Balmer lines: a central component with a broad-blue wing, and a boxy component with time-variable blue and red shoulders. The Hα emission profile is well modelled using a circular accretion disc component, and a blue-shifted double Gaussian which may indicate a partially obscured outflow. Weak narrow lines, together with the previously flat light curve, suggest that this object represents a dormant galactic nucleus which has recently been re-activated. Our time-series modelling of the Balmer lines suggests that this is connected to a disturbance in the disc morphology, and we speculate this could involve a sudden violent event such as a tidal disruption event involving the central supermassive black hole, though this cannot be confirmed, and given an estimated black hole mass of $\gtrsim 10^7$–$10^8\,\mathrm{M_\odot}$ instabilities in an existing disc may be more likely. Although we find that the redshifts of AT2017bcc ($z = 0.13$) and G274296 ($z > 0.42$) are inconsistent, this event adds to the growing diversity of both nuclear transients and multimessenger contaminants.

Key words: black hole physics – gravitational waves – galaxies: active – transients: tidal disruption events.

1 INTRODUCTION

It is now established that most galaxies host a central supermassive black hole (SMBH) (Magorrian et al. 1998; Kormendy & Ho 2013). Accretion onto the SMBH can allow a galactic nucleus to outshine its host. Flickering like candles, these active galactic nuclei (AGN) vary in luminosity over time typically at the level of a few tenths of a magnitude as the rate of their accretion changes. This emission illuminates gas hundreds of light years from the SMBH, producing narrow-line spectral features. In some AGN, Doppler-broadened emission is also visible, arising from fast-moving gas surrounding the central accretion disc. In the optical, this is mainly visible in the Balmer lines. While almost all AGN show variable luminosity and narrow-line emission, they are categorized based on whether the broad-line region is visible. Type I AGN show both

broad- and narrow-line features, while Type II AGN lack the broad-line component. This is attributed to a viewing-angle effect, with the broad line region obscured by a dusty torus in Type II AGN (Antonucci 1993; Urry & Padovani 1995).

Due to their persistent variable emission, AGN have historically been treated as contaminants during searches for transient objects. However, with the rise of wide-field sky surveys and automated source detection, we have been able to uncover the more unusual behaviour of nuclear emitters. For example, some AGN have been seen to transition from Type I and Type II, or vice versa, between epochs. These are known as changing-look or changing-state AGN and such objects challenge the paradigm that the difference between the types is purely viewing angle. Though we have observations dating back to the 1970s (Khachikian & Weedman 1971; Antonucci & Cohen 1983), they have been detected more frequently in the last decade (LaMassa et al. 2014; Lawrence et al. 2016; Runnoe et al. 2016; MacLeod et al. 2019; Ricci & Trakhtenbrot 2023).

We have also learned that AGN are not the only source of luminous emission from galactic nuclei. All SMBHs can produce flares by tidally disrupting stars that wander too close, even those which are non-accreting or 'quiescent'. The existence of such tidal disruption events (TDEs) was proposed in the 1970s and 80s (Hills 1975; Rees 1988), and the first candidates were identified in the late 1990s (Komossa & Bade 1999). Since then, we have detected almost 100 TDEs and broadly classified them based on whether they radiate in the X-ray (Auchettl, Guillochon & Ramirez-Ruiz 2017; Sazonov et al. 2021), optical (Gezari et al. 2012; Arcavi et al. 2014; Holoien et al. 2014; van Velzen et al. 2021), or both and if they produce a relativistic jet (Alexander et al. 2020; Andreoni et al. 2022; Cendes et al. 2022; Pasham et al. 2023). As with AGN, some of this diversity of emission is thought to be a result of viewing angle dependence, arising from a non-spherically symmetric envelope of reprocessing material around the SMBH (Dai et al. 2018).

AGN accretion discs may also contain sources of gravitational-wave (GW) emission. It is expected that galactic nuclei host a dense population of stellar-mass black holes, many of which reside in the plane of the central accretion disc (Morris 1993). Binary black holes (BBHs) in such an environment would merge rapidly due to drag from the surrounding gas (McKernan, Ford & O'Shaughnessy 2020). Shocks in the gas and super-Eddington accretion onto the black holes would also produce a fast, bright electromagnetic (EM) transient (Bartos et al. 2017; McKernan et al. 2019). Thus, these mergers could be multimessenger events, producing both GW and EM emission. A candidate for such an event was reported by Graham et al. (2020), along with the proposal to monitor AGN when searching for future EM counterparts to GW – including BBH – detections.

In this paper, we present observations of a nuclear transient, AT2017bcc, which was first observed as a candidate EM counterpart to a GW detection. We explore the possibility that this is a genuine multimessenger event by re-analysing the GW signal, finding that the GW and EM sources are likely unrelated. However, the EM source itself shows a number of unusual properties that provide insight into the diversity of AGN variability and nuclear transients, and may shed light on the nature of the AGN changing look phenomenon. We have obtained an extensive data set from X-ray to radio, including time series spectroscopy over a period of six years.

In particular, this event is a rare example (unique to our knowledge) of an AGN that is both changing state and a 'double-peaked emitter' (Storchi-Bergmann et al. 1993; Eracleous et al. 1994) with complex broad-line profiles that vary over time (Gezari, Halpern & Eracleous 2007). Double-peaked emitters often exhibit distinct blue and red shoulders in their broad Balmer lines, consistent with an accretion disc origin (Eracleous et al. 1995). Understanding the line profiles and their evolution in AT2017bcc provide new clues to the processes that have switched this AGN on after a period of quiescence.

The paper is structured as follows. In Section 2, we describe the discovery of AT2017bcc and our re-analysis of G274296. We detail our spectroscopic and photometric follow-up in Section 3. Using fits to archival photometry, we examine the host galaxy in Section 4. We interpret the multiwavelength light curve in Section 5. In Section 6, we present our optical spectroscopy and model the emission profiles to infer physical parameters. Finally we discuss our results in Section 7, and conclude in Section 8. Unless otherwise stated, we adopt a flat ΛCDM cosmology with $H_0 = 67.7 \, \mathrm{km\,s^{-1}}$, $\Omega_0 = 0.31$ throughout (Planck Collaboration et al. 2020).

2 DISCOVERY

On 2017 February 17, the LIGO collaboration reported the identification of a candidate signal, labelled G274296 (Shawhan, LIGO Scientific Collaboration & Virgo 2017), during real-time burst analysis. The signal was flagged by the COHERENT WAVEBURST (CWB; Drago et al. 2020) pipeline; designed to identify GW transients in detector streams without prior knowledge of a signal waveform. As such, G274296 did not obviously resemble the typical waveform 'chirp' expected from a binary inspiral (though this could not be ruled out), but was still significant due to its low false alarm rate of ~1 per 2 months.

During the subsequent search for EM counterparts, the Panoramic Survey Telescope and Rapid Response System (Pan-STARRS; Chambers et al. 2016) discovered a bright nuclear transient on 19th February, then dubbed PS17bgn, in the galaxy SDSS J113152.97+295944.8 within the 90 per cent contour of the G274296 skymap (Chambers et al. 2017). It was spectroscopically classified by the Public ESO Spectroscopic Survey of Transient Objects (PESSTO; Smartt et al. 2015) as a Type II superluminous supernova (SLSN-II) due to its broad Hα emission at redshift $z = 0.133$, and corresponding absolute magnitude of -21 (Taddia et al. 2017). The transient was then renamed to SN2017bcc and dropped from the counterpart search. Later re-examination by Sokolovsky et al. (2017) revealed blue optical and near-UV continuum, suggesting high temperatures. They also detected non-thermal X-ray emission. These features are characteristic of TDEs and AGN flares, and though they do not rule out a SLSN-II origin, X-rays have not been detected in the majority of such objects.

Given the uncertainty in the classification of this transient (and the results of our own analysis), we will refer to this source using its pre-classification IAU name AT2017bcc.

2.1 GW analysis

Since AT2017bcc was discovered during optical follow-up of a GW source, we here assess whether the EM transient could be the true counterpart to the GW signal.

As G274296 was identified by a GW pipeline using unmodelled analysis, a distance to the source could not be determined in real time. Burst-style GW signals are expected to originate from stellar core-collapse, thought to be detectable at current GW sensitivity only at kiloparsec-scale distances (Gossan et al. 2016) (though collapse to a rapidly rotating black hole – a collapsar – may be detectable at ~100 Mpc; Gossan et al. 2016). As such, it is unlikely that G274296 is a true burst source, as it would most likely have been accompanied by an easily identifiable nearby supernova. In any case, a GW burst from a stellar core-collapse would not be detectable at the distance of AT2017bcc (625 Mpc) (Gossan et al. 2016). Therefore if G274296 did originate in this way, the EM and GW sources are not associated.

The alternative scenario is that the signal arose from a compact binary merger. A sufficiently massive system may enter the LIGO bandpass only in the final stages of merger, such that the distinctive chirp signal from the inspiral phase goes unseen. This is a plausible origin of an AGN flare-like counterpart, if the merger occurred within an accretion disc around an SMBH. Indeed, the only previous EM candidate for a merger in an AGN disc (Graham et al. 2020) corresponded to one of the most massive BBH mergers detected by LIGO to date, GW190521: a system with a total mass of ~150 M$_\odot$ (Abbott et al. 2020). Under the assumption of a compact binary merger, to determine the source properties of G274296 we carried out a full Bayesian analysis (Veitch et al. 2015) using two state-of-
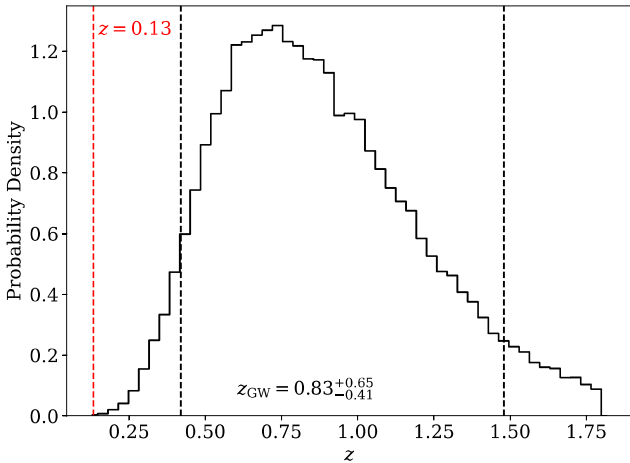
Figure 1. Posterior probability density on redshift from waveform analysis of G274296. The vertical-dashed lines indicate the 1σ region (black) and the spectral redshift of AT2017bcc (red).

the-art waveform models, IMRPhenomXPHM (Pratten et al. 2021) and NRSur7dq4 (Varma et al. 2019), and found it to be consistent with a very massive compact binary with median source-frame progenitor masses of 119(120) $M_\odot$ and 77(73) $M_\odot$ using IMRPhenomXPHM (NRSur7dq4). In this scenario, due to the large component masses, the GW signal is very short in duration ($\ll 1$ s) and dominated by the merger phase, emulating a burst signal, which is consistent with the initial detection by a burst pipeline.

This analysis also produced a luminosity distance posterior, shown in Fig. 1. In this scenario, using the cosmological parameters from Ade et al. (2016) we find the median redshift of G274296 to be $z_{\rm GW} = 0.83^{+0.65}_{-0.41}$. The spectroscopic redshift of AT2017bcc, measured from its narrow [O III] lines, is $z_{\rm EM} = 0.133$ which is outside the 99th percentile of the GW distance posterior. Thus we conclude that, with the absence of further models for the GW signal, AT2017bcc is not a valid EM counterpart for G274296. In the rest of this paper, we will analyse our extensive EM data set and the implications of this very unusual nuclear source for understanding extreme AGN variability.

3 OBSERVATIONS

3.1 Photometry

We observed AT2017bcc during the first optical peak in the *g, r, i* bands using KeplerCam on the 1.2-m telescope at the Fred Lawrence Whipple Observatory (FLWO), and in *g, r, i, z, J, H, K* using the ALFOSC optical imager and spectograph and NOTCam NIR imager and spectrograph on the 2.5-m Nordic Optical Telescope (NOT) at the Roque de los Muchachos Observatory. Bias subtraction and flat fielding were applied either using IRAF or instrument specific pipelines, and sky subtraction was applied to the NOTCam images. Aperture photometry with local background subtraction was performed on all images using PHOTUTILS (Bradley et al. 2021) with field star magnitudes from Pan-STARRS and the Two Micron All Sky Survey (2MASS; Skrutskie et al. 2006) to calculate the photometric zero-points. SDSS reports a petrosian radius of 2.5, 2.4, 1.8, and 2.6 arcsec for the *g, r, i, z* bands, respectively. Thus we decided that an aperture size of 5 arcsec was sufficient to include flux from the compact host galaxy consistently for our optical bands.

We imaged AT2017bcc in *uvw1, uvw2, uvm2, U, B, V* using the Ultraviolet/Optical Telescope (UVOT; Roming et al. 2005) on the

Neil Gehrels *Swift* Observatory. Count rates were obtained using the *Swift* UVOTSOURCE tool and converted to magnitudes (in the AB system) using the UVOT photometric zero-points (Breeveld et al. 2011). The source counts were extracted initially using a source region of 5 arcsec radius. When the count rate dropped to below 0.5 counts per second, we used a source region of 3 arcsec radius. In order to be consistent with the UVOT calibration, these count rates were then corrected to 5 arcsec using the curve of growth contained in the calibration files. Background counts were extracted using a circular aperture of radius 20 arcsec located in a source-free region of the sky.

We also downloaded reduced data from various public surveys covering 2005–2022. Images in *g, r, i, z* were obtained from Pan-STARRS via the PS1 Image Cutout Service; and in *g, r, i* from the Zwicky Transient Facility (ZTF; Bellm et al. 2019), via the NASA/IPAC Infrared Science Archive. These were analysed using PHOTUTILS in order to use a consistent aperture on science images, rather than difference magnitudes, to avoid any unwanted effects from transient contamination in template images.

We acquired survey magnitudes for AT2017bcc in *c, o* from the Asteroid Terrestrial-Impact Last Alert System (ATLAS; Tonry et al. 2018; Smith et al. 2020; Shingles et al. 2021) forced photometry server, using reduced rather than difference images; in *V* from the Catalina Real-time Transient Survey (CRTS; Djorgovski et al. 2011) cone search service; in *W1, W2* from the Near-Earth Object Wide-field Infrared Survey Explorer (*NEOWISE*; Mainzer et al. 2011) via the NASA/IPAC Infrared Science Archive; and in *u, g, r, i, z* from the Sloan Digital Sky Survey (SDSS; Alam et al. 2015).

Fig. 2 shows all of our optical and infrared (IR) photometry in AB magnitudes. The *Swift* UVOT counts had very large uncertainties so were not included in the light curve for visual clarity, but we do show them in Fig. 6.

3.2 X-ray data

X-ray observations were acquired using the X-ray Telescope (XRT) onboard *Swift* over 12 epochs from 2017 March 10 to 2018 March 14. Data were downloaded and analysed using the automated tools provided by the UK *Swift* Science Data Centre (Evans et al. 2007, 2009). We stacked all available data to produce a high-S/N X-ray spectrum from 0.3–10 keV with a total exposure of 20.5 ks, and fit this with both power-law and blackbody models at a redshift $z = 0.133$. The models include both a redshifted and Galactic absorber, using the Tübingen-Boulder ISM absorption model (TBabs; Wilms, Allen & McCray 2000) and the Galactic column from Willingale et al. (2013), fixed at 1.9×10^{20} cm^{-2}. Thus, in the terminology of the XSPEC package, we fit the models TBABS × ZTBABS × ZPOWERLW and TBABS × ZTBABS × ZBBODY. The power law provides an adequate fit to the data, with a w-stat of 197 for 245 degrees of freedom. The blackbody fit is a poor visual match and provides a far inferior fit with a w-stat of 359.

The best-fitting photon index for our preferred power-law model is $\Gamma = 1.54^{+0.14}_{-0.11}$. This is consistent with the lower end of the distribution for AGN, which have a population averaged $\langle \Gamma \rangle \approx 1.7 - 1.8$ (Tozzi et al. 2006; Winter et al. 2009). The fit does not require any intrinsic hydrogen column absorption. The model gives a mean unabsorbed flux $F_X = 1.21 \times 10^{-12}$ erg cm^{-2} s^{-1}. We also produced a light curve binned by visit, finding some indication of fading by a factor ~ 2 between 2017 and 2018, however the significance is only $\approx 1\sigma$, and this is also comparable to the visit-to-visit scatter in the light curve. The count-rate light curve is given in Appendix Table A1, and the light curve and spectrum plots
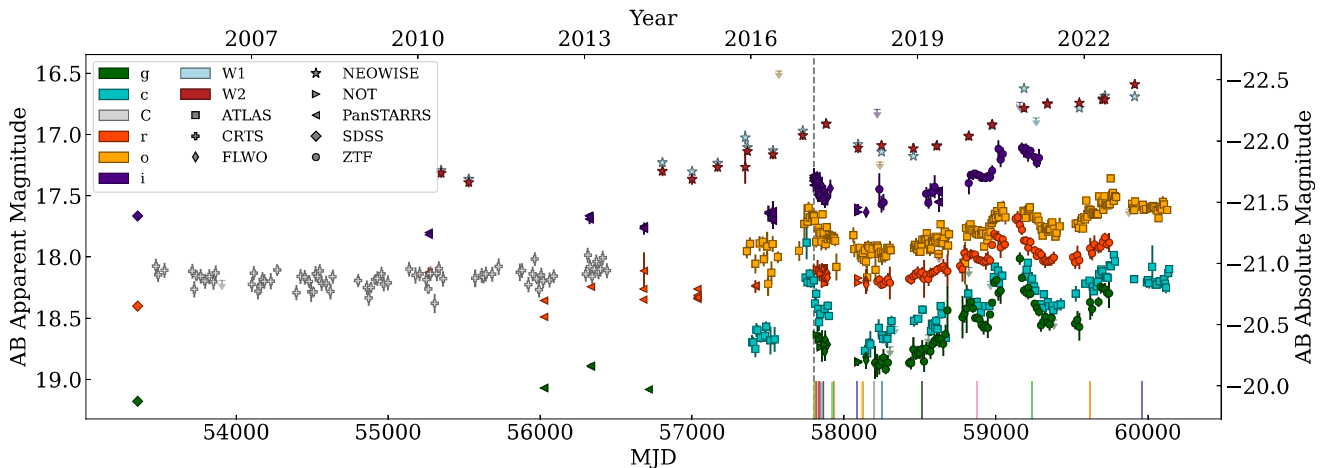
Figure 2. Optical and infrared light curve of AT2017bcc. All magnitudes are corrected for galactic extinction and still include host light. Each point is the result of binning fluxes to a weekly cadence for visual clarity. Epochs below a 5σ detection limit are plotted as upper limits with a lower opacity. The vertical-dashed line indicates the discovery by Pan-STARRS in February 2017. The epochs of spectroscopy are marked below the magnitudes, with the same colours used in Fig. 3.

produced by the XRT online tools are provided Fig. A1 and Fig. A2 respectively.

3.3 Radio data

AT2017bcc was observed by the Jansky Very Large Array (VLA) over 4 logarithmically spaced epochs between 2017 March 21 and 2018 January 17 from 3 to 25 GHz (PI: Alexander). These were reduced using the standard NRAO pipeline in Common Astronomy Software Applications (CASA; McMullin et al. 2007). The observed fluxes are listed in Appendix Table A2. There is no obvious variability at any frequency, with typical flux of $\sim 300\,\mu$Jy. Historical observations from the VLA's FIRST and VLASS surveys contain detections with consistent flux-density as early as 1993, suggesting that these emissions are unrelated to the recent optical flaring. If the radio emission were due to obscured ongoing star formation, the implied star-formation rate (SFR) would be $\sim 9\,M_\odot\,\mathrm{yr}^{-1}$, using the average flux at 5 GHz with the relation from Yun & Carilli (2002). Alternatively, this may indicate historical AGN activity on the time-scale of thousands of years (Hardcastle & Croston 2020).

3.4 Spectra

We obtained 20 epochs of spectroscopy between 2017 February 19 and 2023 January 15. Five epochs were taken with EFOSC2 on the New Technology Telescope (NTT) as part of ePESSTO + and reduced via the PESSTO pipeline (Smartt et al. 2015). We took six with the OSMOS spectograph on the 2.4 m telescope at the MDM Observatory (Martini et al. 2011), three with ALFOSC on the NOT and six at the MMT Observatory (five with Bluechannel and one with Binospec) all of which were debiased, flat-fielded, and cosmic ray corrected using either IRAF or standard PYTHON libraries. Finally, we acquired a spectrum with FORS2 on the Very Large Telescope (VLT) which was reduced using ESO Reflex. Relative flux calibration was achieved for all spectra using standard stars observed with the same instrument setups; calibrated spectra were then rescaled to match contemporaneous photometry. Fig. 3 shows these spectra, further corrected for telluric absorptions and continuum subtracted to emphasize the emission lines.

4 HOST GALAXY

We retrieved archival magnitudes of the host galaxy, SDSS J113152.98+295944.8 (or WISEA J113152.97+295944.9), from a number of catalogs. Optical data were obtained from the SDSS (Alam et al. 2015) in the u, g, r, i, z bands. Near-infrared photometry was available from the 2 Micron All Sky Survey (2MASS; Skrutskie et al. 2006) in J, H, K, and mid-IR from the *WISE* (Wright et al. 2010) in the bands $W1 - 3$. UV data were collected from the GALaxy Evolution eXplorer (*GALEX*; Martin et al. 2005). In all cases, we used the default reported magnitudes from each instrument.

We modelled the resulting SED using PROSPECTOR (Johnson et al. 2021). We used the Prospector-α model setup from Leja et al. (2017), where the free parameters are the total mass formed in the galaxy, the metallicity, the current specific SFR in the last 50 Myr, the widths in time of five equal-mass bins to model the star-formation history, three parameters that control dust absorption by both the interstellar medium and stellar birth clouds, and three parameters governing dust emission. We refer the reader to Leja et al. (2017) for an in-depth discussion of these parameters and their degeneracies. In particular, the default model does not work well for galaxies with a substantial AGN contribution, so we fit additionally for the fraction of IR emission originating from an AGN torus. The model posteriors were explored using EMCEE (Foreman-Mackey et al. 2013). We ran the sampler with various combinations of 32–128 walkers (Goodman & Weare 2010) and chain lengths of $\sim$1000–10 000 steps. We found consistent posterior distributions, suggesting reliable convergence. The resulting corner plot is shown in Fig. A4.

The resulting SED fit is shown in Fig. 4. This is a red galaxy with an old stellar population, with most star formation occurring $\sim$9 Gyr ago, and a present-day SFR of $\sim 1\,M_\odot\,\mathrm{yr}^{-1}$. The *WISE* colours, $W1 - W2 = 0.62 \pm 0.05$ and $W2 - W3 = 1.92 \pm 0.34$, are most consistent with star-forming galaxies. This is in contrast to the majority of TDE host galaxies, which typically have star formation histories peaking $\sim$0.1–1 Gyr ago (French et al. 2020). The PROSPECTOR SFR is significantly lower than that implied by the radio luminosity of this galaxy. To investigate this issue further, we measured the average flux of the narrow [O II] λ3727 line in our spectra and used the calibration of Kennicutt (1998) as an additional SFR indicator. This line was
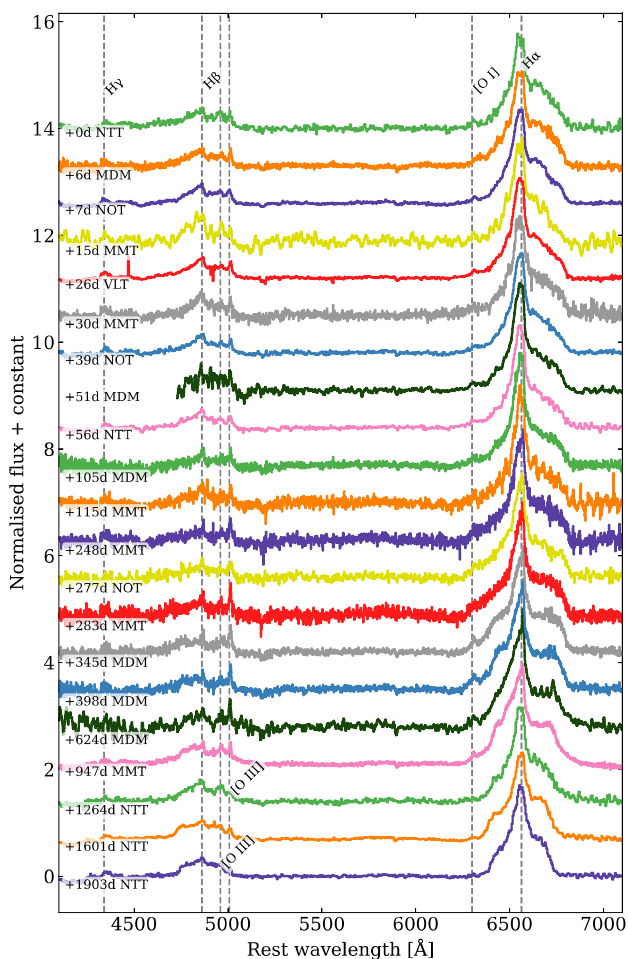
Figure 3. Optical spectroscopic evolution of AT2017bcc, containing 20 epochs from day one (2017 February 19) to day 2157 (2023 January 15) post-discovery. Each epoch is labelled with the rest-frame days since discovery and the telescope/observatory which took the data. All spectra are telluric-corrected, continuum-subtracted, and normalized for visual clarity. Some spectra have been smoothed using a Savitzky–Golay filter.

chosen as it is not blended with any of the complicated broad line profiles from the Balmer series. A luminosity of $\approx 6 \times 10^{39}\,\mathrm{erg\,s^{-1}}$ implies a SFR of $\approx 0.1\,\mathrm{M_\odot\,yr^{-1}}$. This is somewhat lower than the PROSPECTOR SFR, and much lower than the radio-implied SFR. Some of the discrepancy may be due to differences in aperture size between imaging and spectra, though we have attempted to scale our spectra to match in principle the apertures used for photometry. Our estimate from PROSPECTOR may therefore be an overestimate, and the true SFR likely lies somewhere between ~ 0.1–$1\,\mathrm{M_\odot\,yr^{-1}}$. Given the very large discrepancy if we interpret it as star formation, we suggest that the radio emission is more likely related to historical AGN activity (Hardcastle & Croston 2020).

The PROSPECTOR fit prefers a solar or slightly super-solar metallicity, $\log(Z/Z_\odot) = 0.1^{+0.07}_{-0.15}$, and a stellar mass $\log(M_*/M_\odot) = 10.70 \pm 0.08$. Assuming the mean bulge-to-total light ratio for this galaxy mass $B/T \sim 0.7$ (Stone et al. 2018), this implies a SMBH mass of $\approx 1.5 \times 10^8\,\mathrm{M_\odot}$ using the relation of Kormendy & Ho (2013). An SMBH of this mass would disfavour a TDE origin for the variability in AT2017bcc, as this is above the Hills mass for direct capture (no disruption outside the event horizon) of a solar mass star (Hills 1975), unless the BH is rapidly rotating and the star entered on a prograde
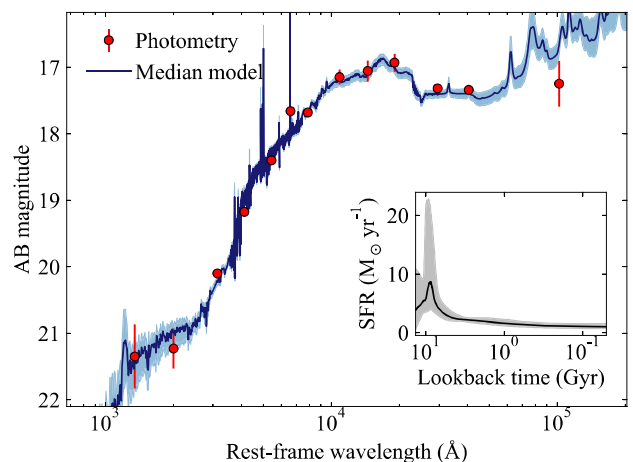

Figure 4. Fit to the archival spectral energy distribution (SED) of the AT2017bcc host galaxy using PROSPECTOR. The inset shows the implied star-formation history. Shaded areas show the 16th and 84th percentiles of the model posteriors.

orbit (Leloudas et al. 2016). However, the bulge mass of this galaxy is consistent with the most massive TDE host in Ramsden et al. (2022), and their flatter BH-bulge relation for TDE host galaxies would suggest a SMBH more like $\sim 10^7\,\mathrm{M_\odot}$.

Our fit does not require the existence of a powerful AGN prior to the onset of variability in 2017. The IR luminosity fraction is $f_{\mathrm{AGN}} = 0.08 \pm 0.02$, that is, a contribution of $\lesssim 10$ per cent to the total IR emission could arise from a pre-existing dusty torus. However, this contribution is above zero at 4σ, indicating that this structure likely does exist, even if it is not illuminated by a large accretion rate onto the central SMBH at that time. Overall, our SED model points to a largely dormant AGN with a SMBH mass in the range of a few $\times 10^7 - 10^8\,\mathrm{M_\odot}$.

5 PHOTOMETRIC ANALYSIS

5.1 Light curve

We have compiled a light curve for AT2017bcc consisting of over 15 yr of survey photometry with almost unbroken coverage, shown in Fig. 2. This photometry includes flux contributions from both the transient/variable nuclear source, and the host galaxy. We show in Appendix Fig. A5 a light curve with host light (from our PROSPECTOR fit) subtracted. If we trust that the pre-flare photometry is free from contamination by any previous variability, the implied optical colour of the flare is apparently constant with $g - r \simeq 0$. However, for the bulk of this analysis we will take the more agnostic approach of using the large aperture photometry without subtracting pre-flare light.

The light curve in Fig. 2 shows two distinct phases separated by the discovery in early 2017. The first phase is one of quiescence, covered by SDSS, CRTS, and Pan-STARRS, which shows negligible change in magnitude over ~ 10 yr. CRTS is particularly well-sampled, showing little deviation ($\sigma = 0.1$ mag) from a C-band apparent magnitude of 18.2 (absolute magnitude of -21.0). Two epochs of *WISE* data in 2010 are also consistent with the first *NEOWISE* magnitudes in 2014, both reporting $W1$ and $W2$-band magnitudes of ~ 17.4 (AB), suggesting very little activity at both optical and infrared wavelengths. However, with sparser time sampling compared to the optical, it is harder to exclude variability pre-2017 in the IR.
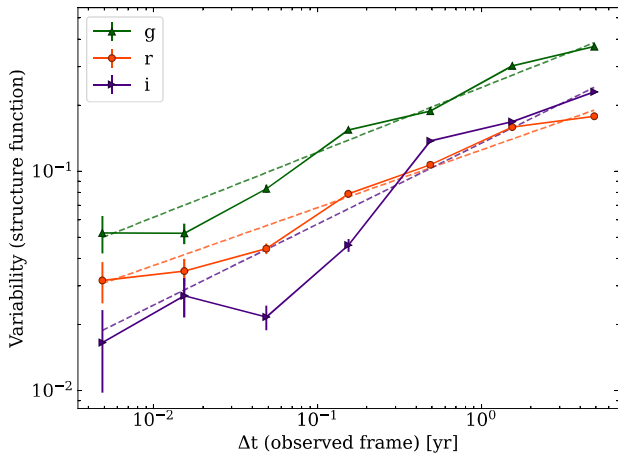
Figure 5. Structure functions, as defined in equation (1), for AT2017bcc in *g*, *r*, *i*, using photometry from 2014 onward with logarithmic time bins. The dashed lines show power-law fits to the structure functions, where *A*, the variability amplitude at 1 yr, and γ, the power-law exponent, are the parameters being optimized. The best fit parameters for each band are as follows *g*: $A = 0.24$, $\gamma = 0.30$; *r*: $A = 0.13$, $\gamma = 0.26$; *i*: $A = 0.13$, $\gamma = 0.37$.
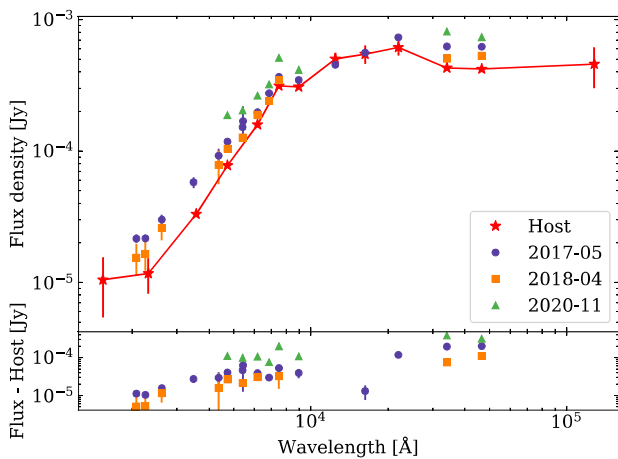

Figure 6. SED of AT2017bcc at multiple epochs. Each point is an average flux from a 3-month time bin centred on the labelled epoch, plotted at the filter's effective wavelength. The archival SDSS, 2MASS, and WISE magnitudes are shown in red (labelled 'Host'). The lower panel shows the same SEDs with the interpolated host magnitudes subtracted. The full SED across all observed wavelengths is shown in Fig. A3.

The flare in early 2017 marks the beginning of a second, more active phase. This phase is well covered by ATLAS, *NEOWISE*, and ZTF, which capture repeated flaring at irregular times and magnitudes. It is difficult to quantify the rise time, but the Pan-STARRS magnitudes in the *r*- and *i*-bands remain constant from the end of the *CRTS* coverage until the first epoch of *ATLAS* photometry. This constrains the optical rise to the ∼200 d gap before the peak in 2017. The first flare reaches a peak *o*-band magnitude of 17.5 in ATLAS, marking a rise of 0.5 mag from the previous year, and then fades back to a magnitude of 18.0 in mid-2018. The object then spends the later two years slowly rising to a second peak in late 2020. Notably, the variability is more pronounced in bluer bands: while the *o*-band returns to its previous peak magnitude, the second *r*- and *g*-band peaks appear to be brighter than the first. This is then followed

by a faster fade and rebrightening throughout 2021 and 2022, and then a third peak in 2023 exceeding the luminosity of the first two.

The second phase rules out a supernova origin for AT2017bcc, as supernovae are not known to rebrighten so dramatically on these time-scales. Some TDEs are known to rebrighten after the initial peak, though they do so on time-scales shorter than a year, and have not been observed to rise back to the original peak luminosity. Additionally, a third peak in the light curve is unprecedented for the known sample of TDEs (Yao et al. 2023). However, AGN do exhibit repeated flaring. Therefore, we investigate whether the statistical properties of the variability in AT2017bcc is consistent with an AGN.

5.2 Structure function

To compare the active phase of AT2017bcc's light curve to a typical AGN, we characterize its variability using the structure function, following the definition provided by Schmidt et al. (2010). The variability *V* in a given time bin Δt is defined as

$$V(\Delta t) = \left\langle \sqrt{\frac{\pi}{2}} |\Delta m_{i,j}| - \sqrt{\sigma_i^2 + \sigma_j^2} \right\rangle_{\Delta t}, \tag{1}$$

where $\Delta m_{i,j}$ is the difference in magnitude between observations *i* and *j*, σ_i, and σ_j are the photometric errors on those magnitudes, and $\langle \rangle_{\Delta t}$ signifies the average taken over all epoch pairs *i*, *j* that fall in the bin Δt. Fig. 5 shows this function plotted for the *g*, *r*, *i* bands using photometry from 2014 onward. This covers the epoch of variability, as well as the ambiguous period after the CRTS coverage.

We fit these structure functions with a power law in the form $V = A\Delta t^\gamma$, where *A*, the variability amplitude at 1 yr, and γ, the power-law exponent, are the parameters being optimized. Focusing on the *r*-band to be consistent with Schmidt et al. (2010), we find that $A = 0.13$, $\gamma = 0.26$. This lies within the quasi-stellar object (QSO) region of the parameter space described in Schmidt et al. (2010). The caveat to this analysis is that we have very few cycles of the variability on the longer time-scales, so these results may change over a longer observational baseline.

5.3 SED and IR evolution

Due to the wide range of wavelengths probed by the photometry for this object, we are able to examine its UV–IR SED at multiple epochs. Fig. 6 shows the SED for AT2017bcc at the epochs of the first peak in luminosity, the first minimum, and just after the second peak. The source can be seen clearly above the host at all three epochs, with the largest flux excess in the UV and in the mid-infrared. These features are characteristic of outbursts from galactic nuclei, a population dominated by TDEs and AGN flares, with the mid-IR emission thought to originate from light echoes from pre-existing dust (Mattila et al. 2018; Kool et al. 2020; Jiang et al. 2021; Reynolds et al. 2022).

The IR luminosity begins to increase in 2015/2016, with an eventual rise time on the scale of a year. The first peak in *NEOWISE* occurs when the optical is already fading, potentially lagging the optical peak by ∼6 months. This implies a distance of ∼ 10^{17} cm between the optical and IR emission regions, consistent with the radius of an AGN dusty torus (Hickox & Alexander 2018). Taking the best fit *W1* and *W2* flux from our PROSPECTOR model (consistent with the 2010 magnitudes) and subtracting these from the *WISE* light curves, we see a possible colour change during the flare, becoming bluer in 2017, redder again during 2018, and evolving back towards $W1 - W2 = 0$ during the second optical rise in 2019–2020. This could imply heating of dust by each flare. However, we caveat that
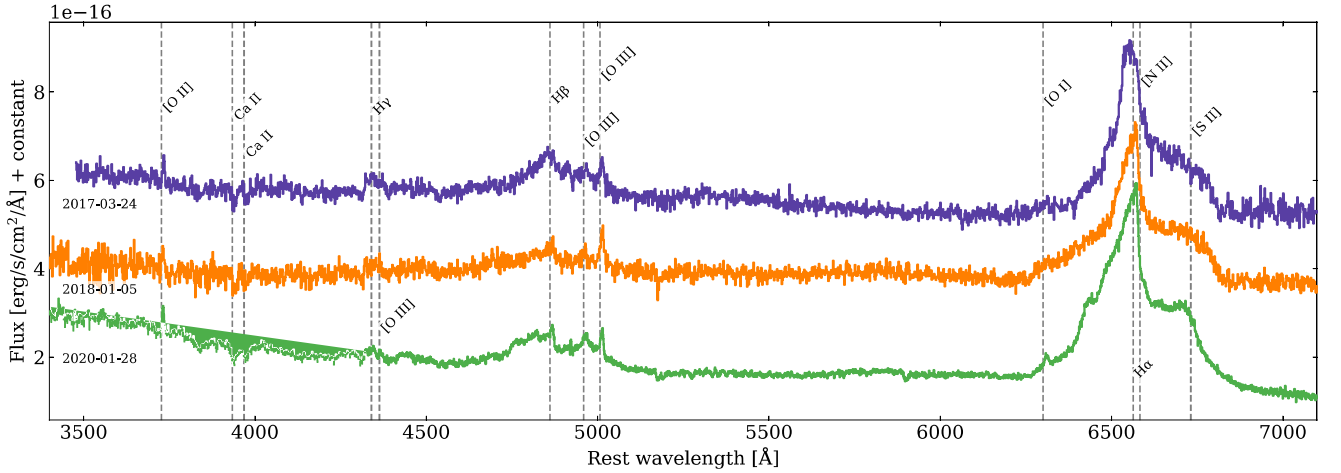
Figure 7. Three representative epochs of spectroscopy for AT2017bcc. All spectra were taken at the MMT observatory, the 2017 and 2018 epochs using Bluechannel, and the 2020 epoch using Binospec. All epochs have been flux-corrected using survey photometry and telluric-corrected. Relevant emission and absorption lines are marked with dashed vertical lines.
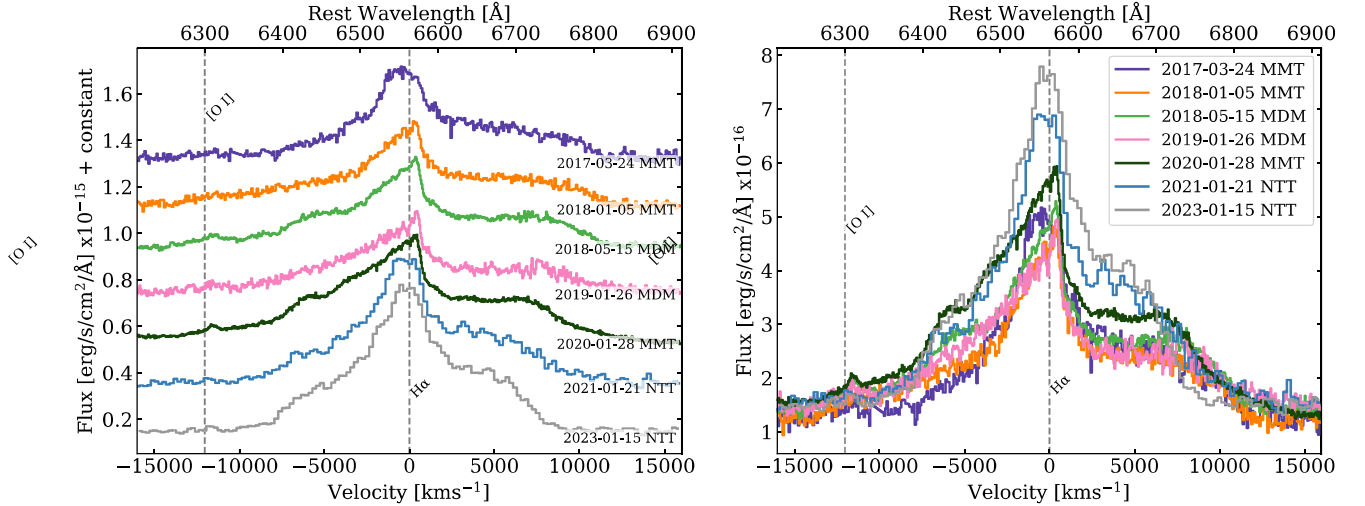

Figure 8. Time-series evolution of the Hα emission profile of AT2017bcc. All epochs have been flux-corrected using survey photometry and telluric-corrected. The left and right panels show the same spectra with and without vertical offsets respectively for visual clarity.

the colour evolution is quite sensitive to the host subtraction, and the implied blackbody temperature of the dust emission is at all times in the range $\approx 900 \pm 150$ K.

We can estimate the bolometric luminosity needed to heat the dust following Somalwar et al. (2022). For a dust temperature of 900 K and a radius of 10^{17} cm and an assumed grain size of 0.1 μm (Draine & Lee 1984), their equation 4 leads to $L_{\rm bol} \sim$ few $\times$ 10^{46} erg s^{-1} assuming a covering factor of 1, or $\sim 10^{45}$ erg s^{-1} for a more realistic covering factor of ~ 0.1 (Ricci et al. 2017).

6 SPECTROSCOPIC ANALYSIS

6.1 Spectral evolution and comparisons

The optical spectra of AT2017bcc show a blue continuum and broad, multicomponent hydrogen emission. Fig. 7 presents three representative epochs of spectroscopy: shortly after discovery, during

the first minimum, and during the rise to the second peak in luminosity.

The most notable difference between these epochs is the evolution of the Hα line profile. The profile in 2017 shows two main components: an asymmetric, very broad component with an excess in flux on the red shoulder, and a narrower component which appears to be blueshifted by ~ 500 kms^{-1}. In 2018, after the initial flare has faded, the narrower component becomes distinctly asymmetric with a blue wing, and peaks at the rest wavelength of 6568 Å. As the luminosity rises to a second peak in 2020, the broad component develops a blue shoulder as the profile becomes overall 'boxy' in shape.

Fig. 8 shows a zoom-in on Hα and its subsequent development over the further 3 yr. Between 2020 and 2021, the red shoulder of the broad component becomes stronger, such that the two wings are once again unequal in height. The relative heights of the blue and red shoulders do not appear to evolve further past 2021. Unfortunately, the spectral resolution of the data after 2020 is not sufficient to
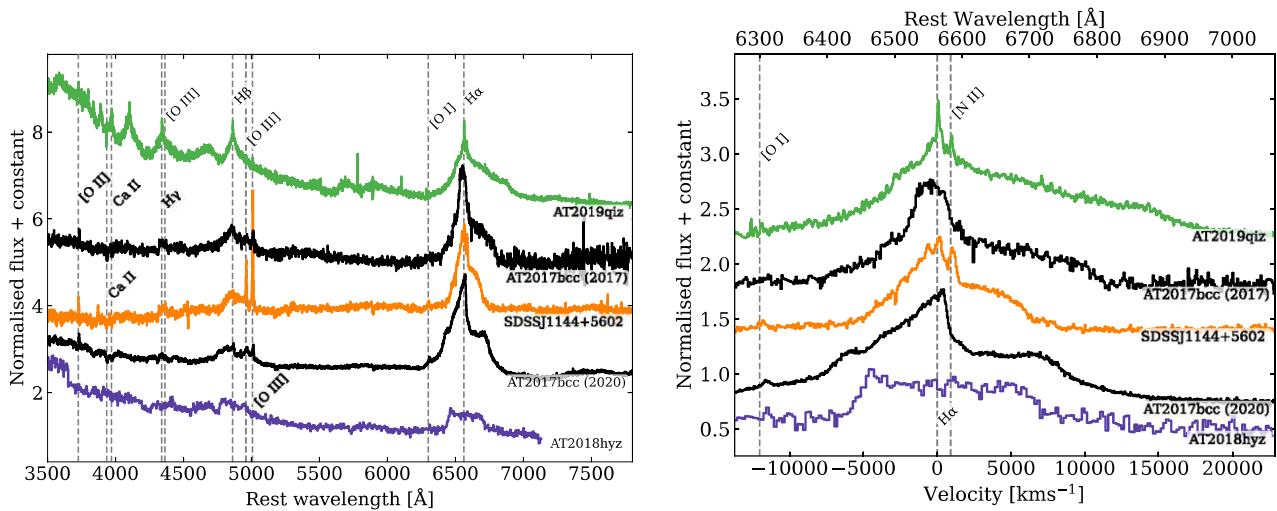
Figure 9. Spectral comparison between two epochs of AT2017bcc (coloured black) and other nuclear transients. The comparison objects were selected from the literature for their similar features to AT2017bcc, and their high signal to noise ratios. All spectra have been normalized for visual clarity. The right panel shows a zoom-in on the H α profiles with alternative normalization, for ease of comparison.
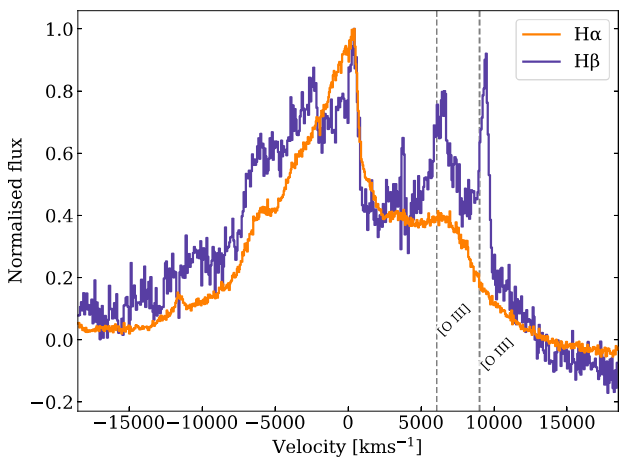
Figure 10. Overplot in velocity space of the H α and H β regions of the 2020 epoch of spectroscopy. The two regions have been normalized to the same height for visual comparison. The narrow [O III] emission lines are marked to distinguish them from the H β profile.

determine whether the narrower component is still asymmetric or simply blueshifted.

Fig. 9 compares the 2017 and 2020 epochs of AT2017bcc to optical spectra from other nuclear transients. The early-time broad component of H α resembles that of SDSS J1144+5602, a double-peaked AGN (Pâris et al. 2017), though the shape of the wings is more similar to those of AT2019qiz, a nearby TDE (Nicholl et al. 2020; Hung et al. 2021). This same broad component in the later profile has much steeper sides, bearing more resemblance to the H α profile of AT2018hyz, a unique TDE with double-peaked emission lines (Gomez et al. 2020; Hung et al. 2020; Short et al. 2020). In the case of AT2018hyz, this broad emission profile has been attributed to an exposed accretion disc.

The narrow component in the later spectrum has a steep drop in flux on the red side, and a shallower slope on the blue side. This is most similar to the central component and blue wing of H α in SDSS

J1144+5602 (though the asymmetry is much more pronounced in AT2017bcc). These comparisons may suggest that the H α profile of AT2017bcc is comprised of a broad, accretion disc-like component similar to some TDEs as well as double-peaked AGN (Eracleous et al. 1994), which has evolved over time; and a narrower, asymmetric 'shark fin' component similar to some double-peaked AGN.

The broad, double-peaked component can also be seen in the H β profile, with the same width in velocity space as in H α, as shown in Fig. 10. There is also an asymmetry in the central component of the H β profile, though its blue shoulder is less smooth. Unlike most AGN, the narrow [O III] emission at 4959 Å and 5007 Å is weak. The [O III] flux appears comparable to the narrow component of H β. As seen in SDSSJ1144+5602, AGN typically have an [O III]/H β flux ratio of $\gg 1$ (Stern & Laor 2012).

6.2 Line profile fitting

We applied the circular accretion disc model from Chen & Halpern (1989) to the double-peaked spectra of AT2017bcc to determine the time-varying accretion disc properties. We fit to normalized spectra, and so this analysis is not sensitive to precise flux calibrations of spectra obtained with different slit widths. We first modelled the high-S/N continuum-subtracted spectrum from 2020 January 28 with the following components: a circular accretion disc model for the H α and H β broad emission-line regions; the narrow emission lines from H α, H β, [S II] λ6717, 6731, [N II] λ6550, 6575, [O I] λ6302, 6366, and [O III] λ5007, 4959; and a broad two Gaussian component close to the H α and H β narrow lines to describe the shark fin feature. A diagram of the emitting regions corresponding to these components is shown in Fig. A8.

The disc models had 2 parameters in common for both the H α and H β emission regions: inclination angle i where 0 degrees is face-on and 90° is edge-on, and a local turbulent broadening parameter σ (km s^{-1}). Three disc parameters were allowed to differ for each of the H α and H β emission regions: the emissivity power-law index q, and the inner and outer dimensionless gravitational radii of the disc ξ_1 and ξ_2. The simple circular disc model did not adequately describe the flat red shoulder of the 2018–2023 spectra, so we enabled a wind
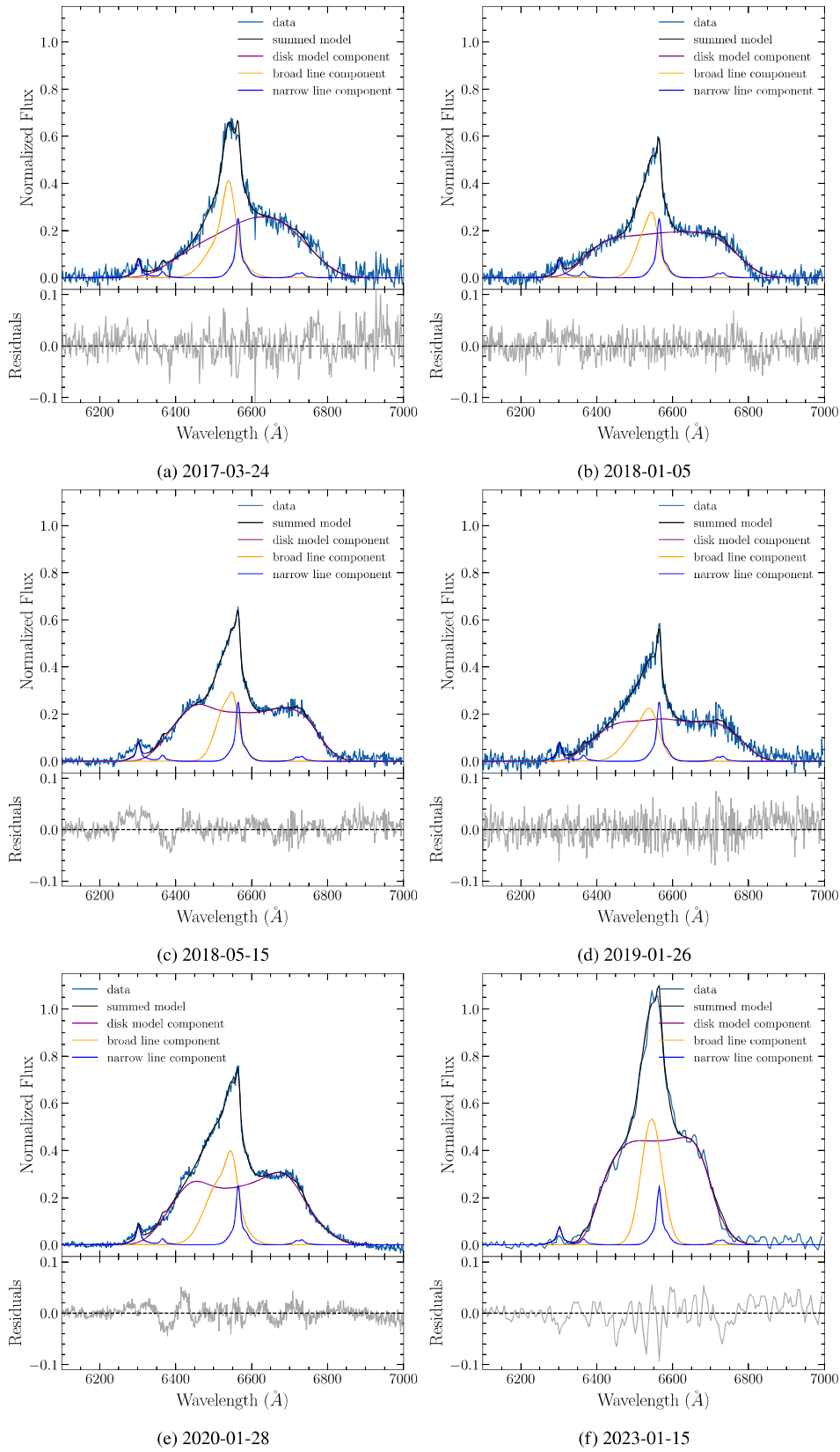
Figure 11. Examples of the best fit Hα disc and broad line models for 6 different spectral epochs of AT2017bcc. The fits were made to continuum-subtracted and telluric-corrected spectra. We have plotted the 1σ uncertainty bands for the best fit model given the distributions of the parameters found by the MCMC modelling, but we note that the range of feasible fits is very narrow for our selected model. The residuals after subtracting both models and the narrow-line component are shown below each profile. A diagram of the emission regions is shown in Appendix A.

(a) Disc inclination angle

(b) Wind amplitude

(c) Spiral arm amplitude

(d) Spiral arm phase
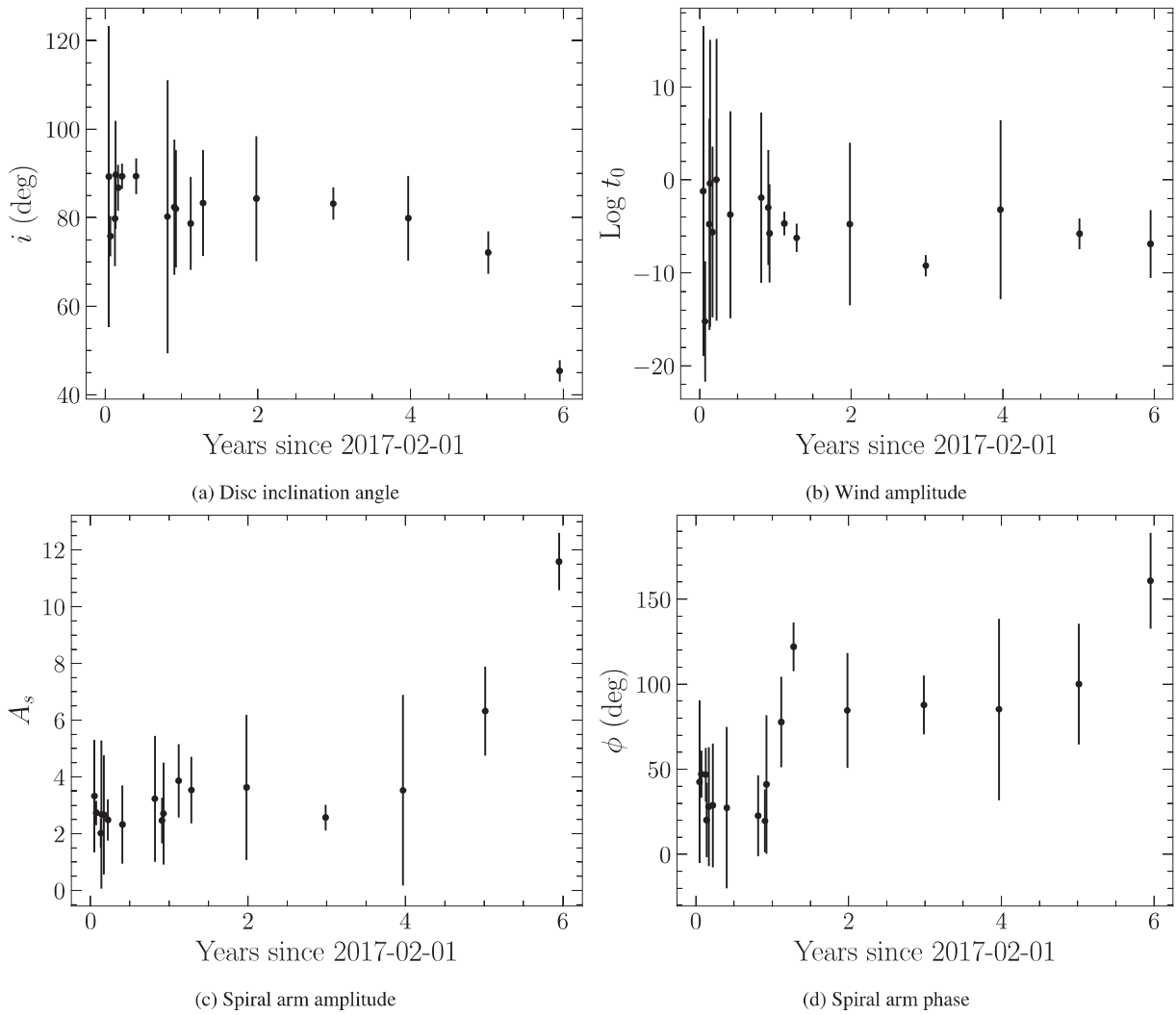
Figure 12. Time series of 4 key parameters from fitting the optical emission profile of AT2017bcc, described in subsection 6.2. These show the inferred evolution of the accretion disc's inclination angle, wind, and spiral arm.

component to the model to increase the 'boxiness' of the double-peaked profile (Nguyen et al. 2018). The disc wind had three free parameters: the opening angle of the wind θ, the wind optical depth τ, and the optical depth normalization t_0 which affects the strength of the wind (Murray & Chiang 1996; Flohic, Eracleous & Bogdanović 2012). Finally, we enabled a single-spiral arm in the accretion disc with free parameters: amplitude A_s (expressed as a contrast ratio relative to the rest of the disc), orientation angle ϕ (deg), width w (deg), and pitch angle ψ (deg). This was required to describe the flux ratio of the red and blue shoulders being >1, as is common amongst disc emitters (e.g. Storchi-Bergmann et al. (2003)).

The narrow lines were fitted with respect to 5 narrow line flux ratio parameters: [N II] $\lambda6583$ /Hα, [S II] $\lambda6731$/Hα, [O I] $\lambda6366$/Hα, [O III] $\lambda5007$/Hβ; Hα/Hβ. The [N II], [S II], [O I], and [O III] doublet flux ratios were fixed to theoretical values of 2.95, 1.3, 0.33, and 2.88 respectively. The narrow lines were described by two-component Gaussians of the same central wavelength with three free parameters which were common for all narrow lines: the width of the first Gaussian component σ_1, the width of the second Gaussian component σ_2, and the flux ratio of the two components f_1/f_2. A two-component Gaussian was chosen because a single Gaussian did not sufficiently describe the peaky line shapes of the [O III] narrow lines which are less contaminated by the disc profile. The redshift of the lines was fit as a single parameter so that the line centroids could be optimized while being tied to the same redshift. The shark fin feature was fitted with a double Gaussian, with each Gaussian having 2 free parameters which are separate for Hα and Hβ: the width σ_b and the rest wavelength offset from the narrow Hα or Hβ line central wavelength Δ. The optimal amplitudes for the sets of narrow lines and broad lines were obtained by solving the covariance matrix for a given set of narrow line, broad line and disc model components, so they were not fitted as parameters during optimization.

We first found a reasonable initial fit using the least-squares optimization implemented in PYTHON using the SCIPY package. We then explored the posteriors using EMCEE (Foreman-Mackey et al. 2013) with 60 walkers initialized at the best fit values from the least-squares fit, distributed according to the 1σ error found from the least-squares covariance matrix. The emcee fitting was run for 5000 iterations with a burn-in time of 4000 iterations. The resulting corner plot is shown in Fig. A7.

For the remainder of the spectra, we fixed the narrow line shapes and amplitudes to the best fit values found from the 2020 January 28 spectrum, but left all broad-line and disc parameters free for refitting. The fitting procedure was repeated using the best fit values from EMCEE fitting of the 2020 January 28 spectrum to initialize the walkers, but with only 2500 iterations and a burn-in time of 2000 iterations, which was the number of iterations required for the walkers to stabilize at their optimal values.

All epochs were well described by our disc+two-Gaussian central broad-line model. The fits to the Hα regions of the spectra are shown in Fig. 11 and the fits to the Hβ regions of the spectra are shown in Appendix Fig. A6. The best fit Hα disc, shark fin, and narrow emission line parameters are shown in Table A3, Table A4, and Table A5 respectively. We note that the absolute flux of the central shark fin structure and the disc profile increased over time relative to the narrow line fluxes. The full-width half maximum (FWHM) of the central outflow structure was approximately 70 Å and showed some changes in morphology through the 6 yr of data (Fig. 11). Evolution in the shape of the shark fin profile, as described by the free parameters for the two-Gaussian model in Appendix Table A4, contributed substantially to changes in the appearance of the left shoulder of the disc profile. Most disc parameters did not evolve substantially over the 6 yr of data, and changes to the width and boxiness of the profile from 2018–2023 could be accounted for solely by changes to the inclination angle and the spiral arm strength and phase.

The disc profiles had a constant emissivity power-law index of $q \sim 1.75$ for both Hα and Hβ emission regions and a constant turbulent broadening parameter of $\sigma \sim 1267$ km s^{-1}. The inner radius stayed constant at $\xi_1 \sim 700$ for the Hα emission region while the outer radius was constant at $\xi_2 \sim 2000$. The best fit inclination angle of the disc stayed within the range of $75 < i < 90°$ in 2017 before decreasing further to $i \sim 45°$ in later epochs, accounting for the decrease in the width of the double-peaked profile (Fig. 12a).

A modest wind of opening angle $\theta \sim 0.8°$ and optical depth $\tau \sim 0.6$ was found to improve the fit to the boxy disc profiles over all epochs (Fig. 12b). The spiral arm parameters evolved over time, with the phase of the arm evolving from $\phi \sim 25$ to $\phi \sim 160$ and the amplitude increasing from $A \sim 2.5$ to $A \sim 11.5$ in later epochs when it became more essential to describe the relative flux of the red and blue peaks of the double-peaked profile (Fig. 12c). The gradual variation in these parameters over multiyear time-scales matches the variability time-scales reported in other double-peaked emitters (Schimoia et al. 2017). The spiral arm had a best fit width of $\sim 50°$, and the pitch angle of the arm was approximately $\sim 25°$.

The narrow line ratios were well within the star-forming regions of the BPT diagram indicating no presence of long-lived AGN activity (Fig. 13). We show only the [N II] $\lambda6583$/Hα and [O I] $\lambda6366$/Hα BPT diagrams because the [S II] $\lambda6731$/Hα fitting may be subject to contamination from the edge of the red disc shoulder. The implied luminosity of the Hα line in our fits is $\sim 10^{40}$ erg s^{-1}, which would correspond to a SFR ~ 0.1 M$_\odot$ yr^{-1}, in agreement with the [O II] line measurement in Section 4, and somewhat lower than the SFR rate estimated from host SED modelling. This suggests that recent AGN activity does not have a large effect on the narrow line fluxes, since a contribution from AGN excitation could only serve to elevate the narrow line fluxes above those expected based on other SF indicators.

In order to see if a disc profile alone could be responsible for both the double-peaked structure and the central shark fin structure, we attempted to fit an alternative model for the 2020 January 28 spectrum which lacked the additional multiGaussian broad line for the shark fin component. This did not produce a high-quality fit because the
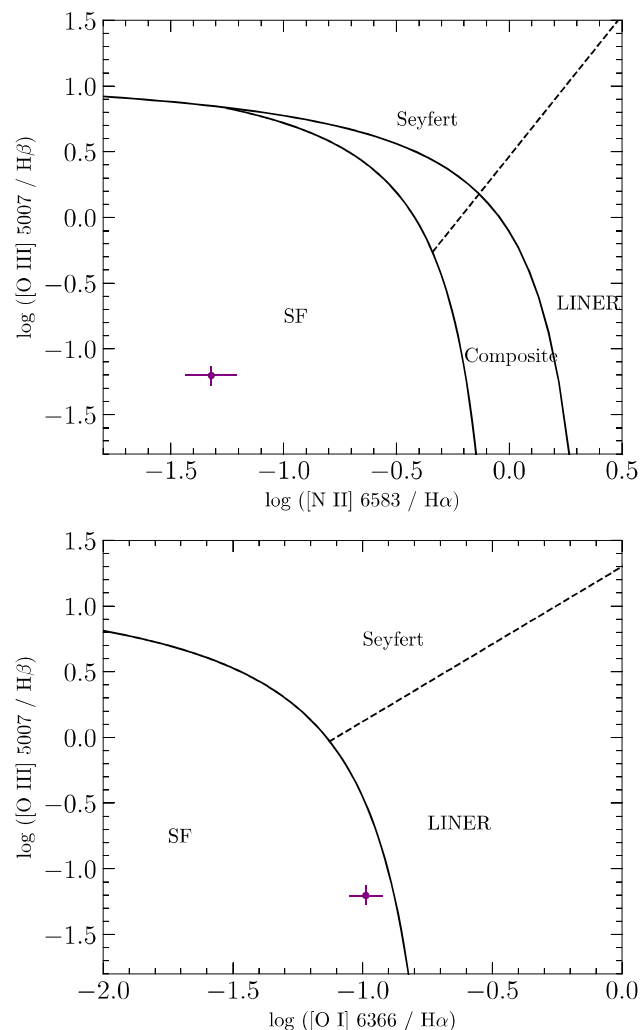

Figure 13. BPT diagrams showing the best fit narrow emission line ratios fit from modelling of the high-S/N 2020 January 28 spectrum.

circular disc model was unable to account for both the shark fin feature and the blue shoulder of the double-peaked spectrum without the additional multiGaussian component.

We caution that the various parameters needed to describe the complex line profile may lead to inevitable degeneracies, especially given the cross-contamination of the evolving shark fin-shaped broad line and the double-peaked disc profile. We also note that it is possible that the two-component Gaussian used to model the narrow lines may be compensating for imperfections in the disc model. However, this should have been mitigated by the requirement that the narrow line morphologies must be consistent across all narrow emission lines, including those which are less contaminated by the disc profile such as [O III]. We also note that the narrow line fluxes and morphologies were fixed after the initial fit to the 2020 January 28 spectrum, and in all cases the disc and outflow model was capable of accurately describing the evolving parts of the spectrum.

In summary, our modelling of the Hα and Hβ broad-line regions finds that the apparent changes to the spectrum over time can be accounted for by: changes to the relative flux of the broad line and narrow line components, changes to the shark fin morphology, and gradual changes to the disc inclination angle along with the spiral arm location and amplitude.
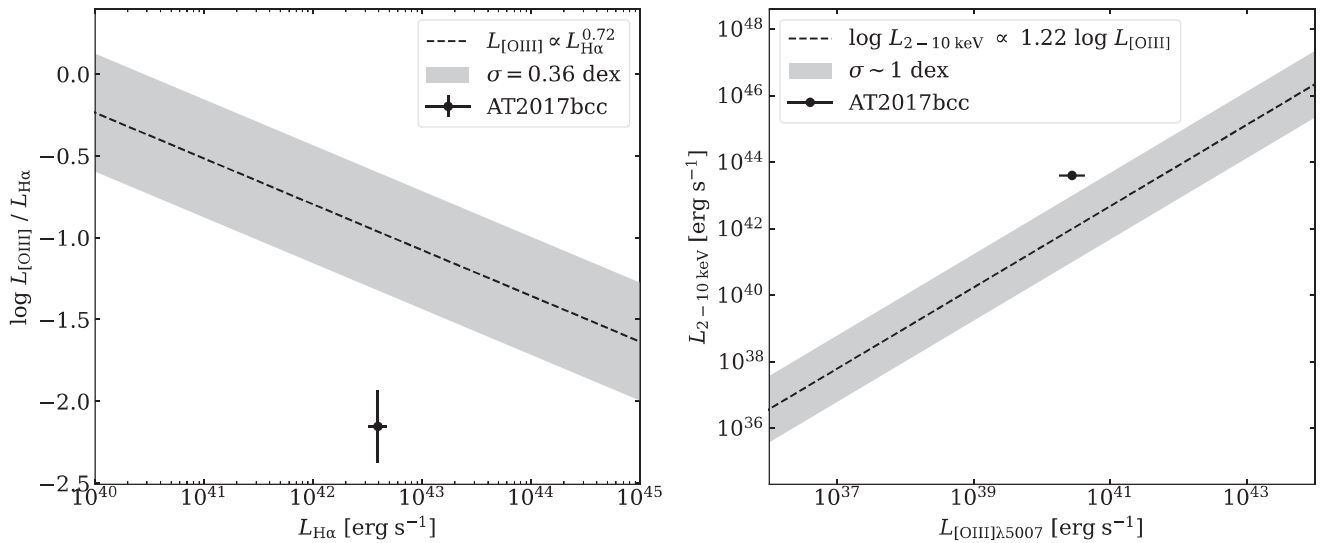
Figure 14. Distributions of [O III] to Hα (left) and X-ray (right) luminosities for AGN, with AT2017bcc marked in black. The distribution in Hα luminosity is shown in Stern & Laor (2012), where they observe a scatter of $\sigma = 0.36$ dex. The distribution in X-ray luminosity is described in Panessa et al. (2006), from which we infer a scatter of $\sigma \sim 1$ dex.

7 DISCUSSION

7.1 Presence of an active SMBH

The repeated rebrightening of its light curve rules out a supernova or a 'typical' TDE as the origin of AT2017bcc. After the original flare in 2017, the luminosity faded for a year, and then rose again to match the first peak, and even exceeded this later on. Even if the first flare was caused by a one-off event, like a TDE, the years-long rise to the later peaks would far exceed the fall-back time for a plausible disruption (Guillochon & Ramirez-Ruiz 2013; Coughlin & Nixon 2022). Although repeating partial TDEs are possible and may have been observed (Payne et al. 2021; Wevers et al. 2023), the light curve of AT2017bcc appears stochastic rather than varying on an orbital period. The most plausible cause of this slower evolution is a gas reservoir in the form of an accretion disc around the central SMBH, that is, a pre-existing but dormant AGN.

This scenario is also supported by a statistical treatment of the light curve. We measured the variability of the recent optical emission from AT2017bcc using its structure function. Power-law fits to this structure function showed best fit parameters for the *r*-band of $A = 0.13$, $\gamma = 0.26$. This is well within the region defined in Schmidt et al. (2010) which separates quasars from other variable sources.

We also find similarities between the spectra of AT2017bcc and those of double-peaked AGN, especially at later times. Once the initial flare had faded the Hα emission profile developed a distinctly asymmetric peak resembling a 'shark fin'. This unusual profile is also seen in SDSS J1144+5602, a known quasar with double-peaked emission features (Pâris et al. 2017).

Double-peaked AGN are a subclass of AGN, spectroscopically selected for their unique emission features. They make up a significant portion of known AGN, accounting for 19 per cent of those observed with ZTF (Ward et al. 2024). Half of this sample show dramatic evolution in the heights of the red/blue peaks in their Hα profiles over time, attributed to the migration of hotspots in the accretion disc. This kind of evolution can also be seen in the wings of AT2017bcc's Hα profile, further implying that it is currently behaving as a double-peaked AGN. These objects typically host higher-mass SMBHs and accrete at larger Eddington ratios, and are more likely to be X-ray and

radio bright (Ward et al. 2024). AT2017bcc seems to represent the discovery of a double-peaked AGN undergoing a dramatic change in its observed properties after a long period of quiescence.

7.2 Narrow line emission

Narrow-line [O III] emission is a defining characteristic of AGN spectra. The strength of [O III] emission around ~ 5000 Å, relative to emission at other wavelengths, is used to categorize active galaxies. One of the most common distinctions is that between high-ionization Seyferts and low-ionization nuclear emission-line regions (LINERs) (Stern & Laor 2013). These groups are usually separated by their position on BPT diagrams (Baldwin et al. 1981), which compare [O III] line strength to [N II], [S II], and [O I]. Alternatively, comparing [O III] emission directly to broad Hα emission (Stern & Laor 2012), or X-ray luminosity (Panessa et al. 2006), describes a continuum of AGN as opposed to a bimodal distribution.

In the case of AT2017bcc, its position on the BPT diagrams in Fig. 13 indicate that its narrow line ratios are characteristic of a star-forming galaxy. It is likely that the observed narrow [O III] emission did not purely arise from star formation, but any AGN contribution is presumably subdominant (otherwise the ratios would lie closer to the AGN region of the BPT diagram).

We also measured the relative strength of its [O III] lines to its broad Hα line and X-ray emission. The relations in Stern & Laor (2012) and Panessa et al. (2006) provide useful points of reference for these measurements, so we have compared our results to them in Fig. 14. It is clear from these metrics that AT2017bcc has much weaker narrow [O III] emission than would be expected for a typical AGN: beyond 3σ for its Hα luminosity, and beyond 1σ for its X-ray luminosity.

7.3 Evidence for phase change

Examples of AGN with weak or non-existent narrow emission lines have recently begun to emerge (Greenwell et al. 2021). These outliers may provide insight into transitional phases of AGN evolution. Two potential scenarios have been proposed to explain this transition.

The first is that the nucleus has been obscured by an influx of material, for example as a result of a recent galaxy merger. This cocoon would prevent the radiation emitted by accretion onto the SMBH from exciting the narrow line regions further out in the galaxy. Eventually, the new material causes the AGN to accrete at a higher rate, increasing the emitted radiation pressure and expelling the obscuring material. There is then a short epoch ($\sim 100\,\mathrm{yr}$), as the newly unobscured light from the nucleus travels to the narrow line regions, when the AGN appears to have very weak [O III] emission. In the case of a recent galaxy merger, we would expect to see signs in the host's morphology, and significant ongoing star formation caused by the material influx (Goulding & Alexander 2009). Our SED fits and radio observations show signs of ongoing star formation (though the radio more likely arises from previous episodes of AGN activity), and higher-resolution imaging could reveal traces of a recent merger. However, the very sudden brightening of the continuum in 2017, and unusual variability of the broad lines, are not naturally accounted for by a scenario of gradually infalling material obscuring the narrow lines, requiring an additional mechanism to fully explain our observations.

The second scenario is that the AGN activity has been recently triggered. This would not require a recent galaxy merger or a cocoon of obscuring material, but instead the serendipitous detection of a significant increase in the accretion rate. AT2017bcc showed negligible variation in luminosity for almost a decade of coverage, prior to the flare in 2017 and subsequent variability. It is well-known that AGN go through phases of increased activity, thought to last on the order of $\sim 10^5\,\mathrm{yr}$ (Schawinski et al. 2015). The increase in luminosity and onset of significant variability in the last few years may mark the beginning of one of these active phases. The fact that the narrow [O III] lines are weak also implies that the central SMBH had been quiescent for at least $\sim 100\,\mathrm{yr}$ (the approximate light travel time to the narrow-line region).

7.4 Origin of initial flare

Flares in galactic nuclei which defy classification are a relatively new class of object (Kankare et al. 2017; Frederick et al. 2021), and in the absence of a single-physical explanation have been dubbed ambiguous nuclear transients (ANTs, Holoien et al. (2022)). Some ANTs have been attributed to gravitational microlensing (Lawrence et al. 2016; Bruce et al. 2017), but in the case of AT2017bcc the clear evolution in the spectral profile rules this out. Double-peaked emission features were also thought to arise from binary AGN (Gaskell & Gaskell 1983). This hypothesis was refuted by Eracleous et al. (1997), and Kelley (2020) describes how double peaks would not be observable in such systems, so we do not consider it here.

We thus conclude that the initial flare most likely signals the beginning of an increase in the rate of accretion onto the central SMBH. This enhanced accretion rate is likely due to a rapid influx of material, either caused by disc instabilities or a disrupted star. As there may have been a dormant AGN disc prior to the flare in 2017, both of these mechanisms are plausible. Interestingly, the only other source for which we could identify a shark fin asymmetry in the central component of Hα is ASASSN-14ko, a periodic nuclear transient in a galaxy hosting dual AGN, and a claimed repeating partial TDE (Payne et al. 2021; Tucker et al. 2021). Here, we explore the possibility that a TDE interacting with an existing accretion disc was the cause of the phase change in AT2017bcc.

Observationally, the flare bears some resemblance to a TDE. Its SED shows a strong blue continuum, with excess emission in the infrared. This is seen in both TDEs and AGN flares (Jiang et al.

2021). The total radiated energy during the initial 2017 flare, $\sim$few $\times$ 10^{51} erg, is also consistent with luminous optical TDEs. Spectral comparisons show that AT2017bcc's broad Hα emission at early times is most similar to TDEs in the literature, while it develops more AGN-like features after the initial flare. The broad component in ASASSN-14ko source could also be modelled with an accretion disc profile, suggesting AT2017bcc and ASASSN-14ko likely share a similar geometry in their line-forming regions. This may strengthen the case for a TDE in both objects, however this does not appear to repeat periodically in AT2017bcc (at least for periods to which we are sensitive, that is, $\lesssim$ a few years). The persistence of the broad line region in the spectra, years after the initial flare, indicates that there may have been a dormant AGN-like accretion disc and broad line region already present. There is a precedent for this kind of event; PS16dtm was a TDE observed in an already active AGN (Blanchard et al. 2017). In that case, X-ray emission from the pre-existing AGN disappeared during the flare, suggesting a disruption or obscuration of the AGN disc.

Fits to the host galaxy's SED show a small (< 10 per cent) AGN contribution to the IR luminosity. The host appears to contain an SMBH in the range of a few $\times 10^7 - 10^8\,M_\odot$, which straddles the Hills mass for a solar-type star. Thus a TDE origin would require either a rather massive star, or for the SMBH to exist in the lower ($< 10^8\,M_\odot$) part of this range, or to be rapidly rotating. While these conditions are not impossible, it is potentially more likely that other AGN flaring mechanisms are driving the recent activity. In particular, the bolometric luminosity $\sim 10^{45}$–10^{46} erg s^{-1} implied by the IR flare is challenging for TDE models. Therefore, even if a TDE was the initial trigger, the bulk of the luminosity produced since 2017 would likely arise from re-activation of a pre-existing disc, rather than accretion of the disrupted star.

8 CONCLUSIONS

We have conducted an extensive study of a nuclear transient, AT2017bcc, discovered by Pan-STARRS (Chambers et al. 2017). As it was found during the counterpart search for a GW signal, G274296 (Shawhan et al. 2017), we explored the possibility that this was a genuine multimessenger event. Although we found the two signals to be likely unrelated, AT2017bcc was unique enough to study in its own right. We thus presented photometric follow-up in the radio, UV, optical, infrared, and X-ray as well as optical spectroscopy.

Modelling archival SDSS magnitudes with PROSPECTOR showed the host to be a red galaxy with an old stellar population, and suggested the presence of a dormant AGN with a SMBH mass of a few $10^7 - 10^8\,M_\odot$. Before it was discovered in 2017 the galaxy showed very little activity, varying in luminosity by <0.1 mags in survey photometry. This historical quiescence was also shown in the weak [O III] emission in recent spectra, which implied that the narrow-line emitting regions of the AGN had not been illuminated for at least $\sim 100\,\mathrm{yr}$.

The flare which marked the discovery of AT2017bcc in 2017 was a long-lived nuclear transient with a strong blue continuum and broad Hα emission. Since then, it has re-brightened multiple times on variable time-scales. In some bands the subsequent peaks were greater in luminosity than the first. We calculated the structure function of this variability, and found it to be consistent with the observed quasar population (Schmidt et al. 2010).

The broad spectral features resembled both TDEs (Nicholl et al. 2020; Short et al. 2020) and double-peaked AGN (Eracleous et al. 1994), with an asymmetrical central component and a boxy broad

component. These features showed evolution in their shape for years after the first luminosity peak. We modelled this spectral evolution using a circular accretion disc with a wind and a single-spiral arm, and a double Gaussian representing a partially obscured outflow. This analysis suggested that the changing profiles were driven by a precession of the disc's inclination, the strength and location of the spiral arm, and the morphology of the outflow.

We conclude that the counterpart search in 2017 serendipitously caught the re-ignition of an AGN which had been dormant for at least a century. A plausible cause of the boosted accretion onto the SMBH is a TDE, or another dramatic event which appears to have disturbed the pre-existing accretion disc.

DATA AVAILABILITY

All data in this paper will be made publicly available via WISeREP (Yaron & Gal-Yam 2012).

REFERENCES

Abbott R. et al., 2020, Phys. Rev. Lett., 125, 101102
Ade P. A. R. et al., 2016, A&A, 594, 13
Alam S. et al., 2015, ApJS, 219, 12
Alexander K. D., van Velzen S., Horesh A., Zauderer B. A., 2020, Space Sci. Rev., 216, 81
Andreoni I. et al., 2022, Nature, 612, 430
Antonucci R., 1993, ARA&A, 31, 473
Antonucci R. R. J., Cohen R. D., 1983, ApJ, 271, L564
Arcavi I. et al., 2014, 38, ApJ, L793
Auchettl K., Guillochon J., Ramirez-Ruiz E., 2017, ApJ, 838, L149
Baldwin J. A., Phillips M. M., Terlevich R., Baldwin J. A., Phillips M. M., Terlevich R., 1981, PASP, 93, 5
Bartos I., Kocsis B., Haiman Z., Márka S., 2017, ApJ, 835, L165
Bellm E. C. et al., 2019, PASP, 131, 018002
Blanchard P. K. et al., 2017, ApJ, 843, L106
Bradley L. et al., 2021, astropy/photutils: 1.1.0. Zenodo
Breeveld A. A., Landsman W., Holland S. T., Roming P., Kuin N. P. M., Page M. J., 2011, in McEnery J. E., Racusin J. L., Gehrels N., eds,

American Institute of Physics Conference Series Vol. 1358, Gamma Ray Bursts 2010. p. 373

Bruce A. et al., 2017, MNRAS, 467, stx168

Cendes Y. et al., 2022, ApJ, 938, L28

Chambers K. C. et al., 2016, preprint,arXiv:1612.05560

Chambers K. C. et al., 2017, GCN, 20699, 1

Chen K., Halpern J. P., 1989, ApJ, 344, L115

Coughlin E. R., Nixon C., 2022, MNRAS, 517, 26

Dai L., McKinney J. C., Roth N., Ramirez-Ruiz E., Miller M. C., 2018, ApJL, 859, L20

Djorgovski S. G. et al., 2011, Proc. Int. Astron. Un., 7, 306

Drago M. et al., 2020, SoftwareX, 14 , 100678

Draine B. T., Lee H. M., 1984, ApJ, 285, L89

Eracleous M., Halpern J. P., Eracleous M., Halpern J. P., 1994, ApJS, 90, 1

Eracleous M., Livio M., Halpern J. P., Storchi-Bergmann T., Eracleous M., Livio M., Halpern J. P., Storchi-Bergmann T., 1995, ApJ, 438, L610

Eracleous M., Halpern J. P., Gilbert A. M., Newman J. A., Filippenko A. V., 1997, ApJ, 490, L216

Evans P. A. et al., 2007, A&A, 469, 379

Evans P. A. et al., 2009, MNRAS, 397, 1177

Flohic H. M., Eracleous M., Bogdanović T., 2012, ApJ, 753, L133

Foreman-Mackey D., Hogg D. W., Lang D., Goodman J., 2013, PASP, 125, 306

Frederick S. et al., 2021, ApJ, 920, L56

French K. D., Wevers T., Law-Smith J., Graur O., Zabludoff A. I., 2020, Space Science Rev., 216, 32

Gaskell C. M., Gaskell M. C., 1983, LIACo, 24, 473

Gezari S., Halpern J. P., Eracleous M., 2007, ApJS, 169, 167

Gezari S. et al., 2012, Nature, 485, 217

Gomez S. et al., 2020, MNRAS, 497, 1925

Goodman J., Weare J., 2010, Commun. Appl. Math. Comput. Sci., 5, 65

Gossan S. E., Sutton P., Stuver A., Zanolin M., Gill K., Ott C. D., 2016, Phys. Rev. D, 93, 042002

Goulding A. D., Alexander D. M., 2009, ASPC, 408, 59

Graham M. et al., 2020, Phys. Rev. Lett., 124, 251102

Greenwell C., Gandhi P., Stern D., Boorman P., Toba Y., Lansbury G., Mainieri V., Desira C., 2021, MNRAS, 503, 80

Guillochon J., Ramirez-Ruiz E., 2013, ApJ, 767, L25

Hardcastle M., Croston J., 2020, New Astron. Rev., 88, 101539

Hickox R. C., Alexander D. M., 2018, ARA&A, 56, 625

Hills J. G., 1975, Nature, 254, 295

Holoien T. W. et al., 2014, MNRAS, 445, 3263

Holoien T. W.-S. et al., 2022, ApJ, 933, L196

Hung T. et al., 2020, ApJ, 903, L31

Hung T. et al., 2021, ApJ, 917, L9

Jiang N. et al., 2021, ApJS, 252, 32

Johnson B. D., Leja J., Conroy C., Speagle J. S., 2021, ApJS, 254, 22

Kankare E. et al., 2017, Nature Astron., 1, 865

Kelley L. Z., 2020, MNRAS, 500, 4065

Kennicutt R. C. Jr, 1998, ARA&A, 36, 189

Khachikian E. Y., Weedman D. W., 1971, ApJ, 164, L109

Komossa S., Bade N., 1999, A&A, 343, 775

Kool E. C. et al., 2020, MNRAS, 498, 2167

Kormendy J., Ho L. C., 2013, ARA&A, 51, 511

LaMassa S. M. et al., 2014, ApJ, 800, L144

Lawrence A. et al., 2016, MNRAS, 463, 296

Leja J., Johnson B. D., Conroy C., van Dokkum P. G., Byler N., 2017, ApJ, 837, L170

Leloudas G. et al., 2016, Nature. Astron., 1, 0002

MacLeod C. L. et al., 2019, ApJ, 874, L8

Magorrian J. et al., 1998, AJ, 115, 2285

Mainzer A. et al., 2011, ApJ, 731, L53

Martin D. C. et al., 2005, ApJ, 619, L1

Martini P. et al., 2011, PASP, 123, 187

Mattila S. et al., 2018, Science, 361, 482

McKernan B. et al., 2019, ApJ, 884, L50

McKernan B., Ford K. E., O'Shaughnessy R., 2020, MNRAS, 498, 4088

McMullin J. P., Waters B., Schiebel D., Young W., Golap K., 2007, in Shaw R. A., Hill F., Bell D. J., eds, Astronomical Society of the Pacific Conference Series Vol. 376, Astronomical Data Analysis Software and Systems XVI. p. 127

Morris M., 1993, ApJ, 408, L496

Murray N., Chiang J., 1996, Nature, 382, 789

Nguyen K., Bogdanović T., Runnoe J. C., Eracleous M., Sigurdsson S., Boroson T., 2018, ApJ, 870, L16

Nicholl M. et al., 2020, MNRAS, 499, 482

Panessa F., Bassani L., Cappi M., Dadina M., Barcons X., Carrera F. J., Ho L. C., Iwasawa K., 2006, A&A, 455, 173

Pasham D. R. et al., 2023, Nature Astron., 7, 88

Payne A. V. et al., 2021, ApJ, 910, L125

Planck Collaboration et al., 2020, A&A, 641, 6

Pratten G. et al., 2021, Phys. Rev. D, 103, 104056

Pâris I. et al., 2017, A&A, 597, 79

Ramsden P., Lanning D., Nicholl M., McGee S. L., 2022, MNRAS, 515, 1146

Rees M. J., 1988, Nature, 333, 523

Reynolds T. M., Mattila S., Efstathiou A., Kankare E., Kool E., Ryder S., Peña-Moñino L., Pérez-Torres M. A., 2022, A&A, 664, 158

Ricci C., Trakhtenbrot B., 2023, Nature Astron., 7, 1282

Ricci C. et al., 2017, Nature, 549, 488

Roming P. W. A. et al., 2005, Space Sci. Rev., 120, 95

Runnoe J. C. et al., 2016, MNRAS, 455, 1691

Sazonov S. et al., 2021, MNRAS, 508, 3820

Schawinski K., Koss M., Berney S., Sartori L. F., 2015, MNRAS, 451, 2517

Schimoia J. S., Storchi-Bergmann T., Winge C., Nemmen R. S., Eracleous M., 2017, MNRAS, 472, 2170

Schmidt K. B., Marshall P. J., Rix H.-W., Jester S., Hennawi J. F., Dobler G., 2010, ApJ, 714, L1194

Shawhan P., Virgo, LIGO Scientific Collaboration, , 2017, GRB Coordinates Network, 20689, 1

Shingles L. et al., 2021, Transient Name Server AstroNote, 7, 1

Short P. et al., 2020, MNRAS, 498, 4119

Skrutskie M. F. et al., 2006, AJ, 131, 1163

Smartt S. J. et al., 2015, A&A, 579, 40

Smith K. W. et al., 2020, PASP, 132, 085002

Sokolovsky K., Wyrzykowski L., Hamanowicz A., Gromadzki M., 2017, ATel, 10177, 1

Somalwar J. J., Ravi V., Dong D., Graham M., Hallinan G., Law C., Lu W., Myers S. T., 2022, ApJ, 929, L184

Stern J., Laor A., 2012, MNRAS, 426, 2703

Stern J., Laor A., 2013, MNRAS, 431, 836

Stone N. C., Generozov A., Vasiliev E., Metzger B. D., 2018, MNRAS, 480, 5060

Storchi-Bergmann T., Baldwin J. A., Wilson A. S., Storchi-Bergmann T., Baldwin J. A., Wilson A. S., 1993, ApJL, 410, L11

Storchi-Bergmann T. et al., 2003, ApJ, 598, L956

Taddia F. et al., 2017, GRB Coordinates Network, 20708, 1

Tonry J. L. et al., 2018, PASP, 130, 064505

Tozzi P. et al., 2006, A&A, 451, 457

Tucker M. A. et al., 2021, MNRAS, 506, 6014

Urry C. M., Padovani P., 1995, PASP, 107, 803

Varma V., Field S. E., Scheel M. A., Blackman J., Gerosa D., Stein L. C., Kidder L. E., Pfeiffer H. P., 2019, Phys. Rev. Research., 1, 033015

Veitch J. et al., 2015, Phys. Rev. D, 91, 042003

van Velzen S. et al., 2021, ApJ, 908, L4

Ward C. et al., 2024, ApJ, 961, 172

Wevers T. et al., 2023, ApJ, 942, L33

Willingale R., Starling R. L. C., Beardmore A. P., Tanvir N. R., O'Brien P. T., 2013, MNRAS, 431, 394

Wilms J., Allen A., McCray R., 2000, ApJ, 542, L914

Winter L. M., Mushotzky R. F., Reynolds C. S., Tueller J., 2009, ApJ, 690, L1322

Wright E. L. et al., 2010, AJ, 140, 1868

Yao Y. et al., 2023, ApJL, 955, L6

Yaron O., Gal-Yam A., 2012, PASP, 124, 668

Yun M. S., Carilli C. L., 2002, ApJ, 568, L88

APPENDIX A: ADDITIONAL PLOTS AND TABLES

Table A1. X-ray light curve for AT2017bcc. The conversion from counts to flux (unabsorbed, 0.3–10 keV) for the best fit power-law model is 4.21×10^{-11} erg cm^{-2} ct^{-1}.

MJD	Counts [sec^{-1}]
57822.917	$0.03120^{+0.01125}_{-0.00909}$
57822.921	$0.03858^{+0.01384}_{-0.01118}$
57822.925	$0.04309^{+0.01532}_{-0.01239}$
57822.928	$0.03553^{+0.01150}_{-0.00947}$
57822.990	$0.04266^{+0.01111}_{-0.01111}$
57843.703	$0.04142^{+0.01485}_{-0.01200}$
57843.708	$0.03251^{+0.01192}_{-0.00963}$
57843.714	$0.02923^{+0.00721}_{-0.00721}$
57850.483	$0.02779^{+0.00830}_{-0.00693}$
57853.145	$0.04136^{+0.01084}_{-0.01084}$
57859.458	$0.02458^{+0.00573}_{-0.00573}$
57864.504	$0.04424^{+0.01584}_{-0.01281}$
57864.510	$0.02696^{+0.00916}_{-0.00748}$
57864.570	$0.03244^{+0.01163}_{-0.00940}$
57864.576	$0.02479^{+0.00772}_{-0.00641}$
57871.080	$0.02881^{+0.00858}_{-0.00717}$
57871.415	$0.06136^{+0.02192}_{-0.01771}$
57871.419	$0.03210^{+0.01153}_{-0.00932}$
57878.319	$0.03748^{+0.01348}_{-0.01089}$
57878.324	$0.03795^{+0.01366}_{-0.01104}$
57878.330	$0.02818^{+0.00926}_{-0.00774}$
57942.427	$0.02704^{+0.00984}_{-0.00795}$
57942.432	$0.04365^{+0.01066}_{-0.01066}$
57942.493	$0.02134^{+0.00732}_{-0.00598}$
57942.498	$0.05483^{+0.01342}_{-0.01342}$
57949.618	$0.02670^{+0.00662}_{-0.00662}$
57955.988	$0.02106^{+0.00540}_{-0.00540}$
58191.653	$0.01857^{+0.00581}_{-0.00482}$

Table A2. Radio observations of AT2017bcc.

MJD	Frequency (GHz)	F (μJy)	dF (μJy)
57833	4.999	354.2	22.9
57833	7.099	358.2	18.1
57833	19.199	173.6	41.7
57833	24.499	140.5	48.0
57835	2.679	373.8	46.8
57835	3.523	366.6	33.4
57835	4.999	422.8	25.5
57835	7.099	378.5	16.3
57835	8.549	366.5	17.0
57835	10.999	314.5	13.6
57835	13.499	256.7	12.3
57835	15.999	222.9	15.0
57869	2.679	212.1	74.1
57869	3.523	309.6	30.8
57869	4.999	357.7	35.5
57869	7.099	340.7	25.3
57869	8.549	326.8	19.5
57869	10.999	305.1	15.2
57869	13.499	282.4	13.5
57869	15.999	271.4	16.7
57934	2.679	375.1	35.3
57934	3.523	375.5	23.8
57934	4.999	350.7	23.0
57934	7.099	307.5	24.5
57934	8.549	351.3	24.1
57934	10.999	322.0	19.5
57934	13.499	325.2	33.2
57934	15.999	321.9	36.3
58135	2.679	332.1	26.0
58135	3.523	345.2	13.3
58135	4.999	372.9	26.1
58135	7.099	336.8	20.1
58135	8.549	311.7	19.5
58135	10.999	269.1	17.4
58135	13.499	286.1	18.8
58135	15.999	295.0	19.6

Table A3. Best fit disc parameters from modelling the Hα and Hβ broad-line regions with the circular accretion disc model from Chen & Halpern (1989). We show the following Hα disc parameters: inner radius ξ_1, outer radius ξ_2, turbulent broadening σ (km s^{-1}), inclination angle i (deg), emissivity power-law index q, spiral arm amplitude expressed as contrast ratio A_s, spiral arm phase ϕ (deg), spiral arm pitch angle ψ (deg), spiral arm width w (deg), wind opening angle θ (deg), log wind amplitude t_0, and wind optical depth τ.

Epoch	ξ_1	ξ_2	σ (km/s)	i (deg)	q	A_s	ϕ (deg)	ψ (deg)	w (deg)	θ (deg)	Log t_0	τ
2017 Feb 19	$700.6^{+18.5}_{-20.3}$	$4.8^{+5.1}_{-7.5}$	$1267.8^{+1.5}_{-1.3}$	$89.3^{+34.0}_{-0.6}$	$1.8^{+1.2}_{-0.8}$	$3.3^{+2.0}_{-2.0}$	$42.5^{+47.5}_{-76.4}$	$40.2^{+43.2}_{-139.6}$	$51.6^{+20.2}_{-22.7}$	$0.7^{+0.4}_{-0.4}$	$-1.2^{+17.7}_{-12.8}$	$0.9^{+0.8}_{-0.9}$
2017 Feb 27	$689.2^{+33.7}_{-25.5}$	$14.8^{+0.9}_{-0.9}$	$1266.2^{+1.1}_{-1.5}$	$75.8^{+4.5}_{-6.3}$	$2.0^{+0.6}_{-0.5}$	$2.7^{+0.4}_{-0.5}$	$47.2^{+13.7}_{-17.3}$	$87.8^{+15.0}_{-5.0}$	$80.4^{+24.1}_{-19.4}$	$0.3^{+0.7}_{-0.7}$	$-15.2^{+6.5}_{-8.2}$	$0.7^{+0.3}_{-0.5}$
2017 Mar 20	$723.4^{+34.6}_{-19.0}$	$10.8^{+12.4}_{-3.2}$	$1267.2^{+1.8}_{-0.8}$	$79.8^{+10.7}_{-29.3}$	$1.9^{+0.2}_{-0.3}$	$2.0^{+0.5}_{-1.2}$	$46.8^{+15.7}_{-91.2}$	$79.9^{+152.6}_{-18.4}$	$59.7^{+39.6}_{-9.9}$	$0.2^{+0.3}_{-1.2}$	$-4.8^{+11.4}_{-13.0}$	$0.5^{+0.1}_{-1.1}$
2017 Mar 24	$701.0^{+27.9}_{-36.1}$	$2.2^{+1.0}_{-18.6}$	$1267.3^{+0.9}_{-1.3}$	$89.7^{+12.2}_{-0.4}$	$2.1^{+1.0}_{-0.4}$	$2.7^{+2.6}_{-2.5}$	$20.1^{+21.8}_{-46.2}$	$64.8^{+71.5}_{-32.7}$	$72.2^{+38.6}_{-33.6}$	$0.7^{+0.8}_{-1.5}$	$-0.4^{+15.4}_{-11.0}$	$0.6^{+0.4}_{-1.1}$
2017 Apr 04	$697.6^{+20.0}_{-5.2}$	$6.9^{+5.5}_{-5.2}$	$1267.8^{+2.1}_{-3.2}$	$86.7^{+5.2}_{-1.5}$	$2.0^{+0.7}_{-0.5}$	$2.7^{+2.1}_{-1.0}$	$27.9^{+34.9}_{-40.7}$	$75.3^{+79.8}_{-40.7}$	$57.2^{+58.4}_{-23.9}$	$0.7^{+0.3}_{-0.2}$	$-5.6^{+9.2}_{-11.0}$	$1.2^{+0.6}_{-0.8}$
2017 Apr 23	$700.4^{+37.5}_{-37.6}$	$2.8^{+1.7}_{-5.8}$	$1267.5^{+2.0}_{-1.7}$	$89.3^{+2.8}_{-1.2}$	$1.7^{+0.9}_{-1.0}$	$2.5^{+0.7}_{-1.0}$	$28.7^{+36.3}_{-59.3}$	$32.2^{+21.8}_{-23.7}$	$53.3^{+26.0}_{-18.0}$	$0.8^{+1.5}_{-3.2}$	$0.0^{+15.2}_{-10.5}$	$0.7^{+0.5}_{-1.6}$
2017 June 29	$704.9^{+30.9}_{-19.2}$	$2.4^{+1.6}_{-10.8}$	$1267.7^{+2.3}_{-2.7}$	$89.4^{+4.0}_{-0.5}$	$1.4^{+1.8}_{-1.6}$	$2.3^{+1.4}_{-0.9}$	$27.3^{+47.4}_{-56.4}$	$34.2^{+33.8}_{-98.4}$	$65.6^{+38.4}_{-55.9}$	$0.7^{+0.3}_{-0.3}$	$-3.7^{+11.1}_{-16.5}$	$1.0^{+1.1}_{-1.1}$
2017 Nov 26	$700.5^{+23.1}_{-25.2}$	$1.5^{+0.9}_{-1.2}$	$1267.7^{+1.0}_{-1.0}$	$80.2^{+30.8}_{-20.7}$	$1.4^{+1.8}_{-1.7}$	$3.2^{+2.2}_{-1.9}$	$22.7^{+23.8}_{-32.6}$	$26.9^{+24.9}_{-139.2}$	$59.9^{+25.4}_{-18.8}$	$1.0^{+0.7}_{-0.6}$	$-1.9^{+19.2}_{-14.9}$	$1.0^{+0.8}_{-1.1}$
2017 Dec 29	$698.0^{+27.8}_{-21.9}$	$1.2^{+0.3}_{-0.4}$	$1268.2^{+1.4}_{-1.4}$	$82.4^{+15.2}_{-8.1}$	$1.3^{+1.5}_{-1.2}$	$2.5^{+0.8}_{-0.9}$	$19.6^{+18.3}_{-22.7}$	$29.1^{+31.0}_{-68.0}$	$47.7^{+25.9}_{-28.6}$	$0.8^{+1.1}_{-1.5}$	$-3.0^{+6.2}_{-3.2}$	$1.1^{+0.8}_{-0.8}$
2018 Jan 05	$707.5^{+23.6}_{-15.1}$	$2.0^{+0.9}_{-2.4}$	$1267.5^{+2.4}_{-1.8}$	$82.0^{+13.2}_{-9.7}$	$1.6^{+1.5}_{-1.2}$	$2.7^{+1.8}_{-1.4}$	$41.1^{+40.7}_{-3.2}$	$20.7^{+28.4}_{-37.1}$	$59.7^{+14.1}_{-11.9}$	$0.7^{+0.9}_{-0.9}$	$-5.7^{+5.3}_{-4.7}$	$0.9^{+0.5}_{-0.8}$
2018 Mar 17	$690.8^{+36.7}_{-33.7}$	$2.7^{+0.8}_{-2.8}$	$1267.7^{+1.6}_{-0.4}$	$78.7^{+10.5}_{-15.3}$	$1.8^{+0.7}_{-0.1}$	$3.9^{+1.3}_{-0.5}$	$77.8^{+26.6}_{-28.7}$	$-27.2^{+72.1}_{-95.5}$	$13.6^{+8.3}_{-65.8}$	$1.0^{+0.3}_{-0.2}$	$-4.7^{+1.2}_{-4.0}$	$0.5^{+0.1}_{-0.2}$
2018 May 15	$703.6^{+46.8}_{-30.9}$	$4.6^{+0.8}_{-0.8}$	$1267.7^{+1.1}_{-1.1}$	$83.3^{+11.9}_{-7.6}$	$0.8^{+1.0}_{-1.8}$	$3.5^{+1.2}_{-1.8}$	$122.0^{+14.3}_{-15.2}$	$25.0^{+5.5}_{-4.9}$	$14.5^{+7.1}_{-5.4}$	$0.1^{+0.1}_{-0.5}$	$-6.2^{+1.5}_{-1.9}$	$0.6^{+0.1}_{-0.3}$
2019 Jan 26	$697.5^{+19.3}_{-16.5}$	$4.0^{+1.7}_{-3.4}$	$1267.0^{+1.8}_{-1.4}$	$84.3^{+14.1}_{-49.7}$	$1.5^{+2.0}_{-1.4}$	$3.6^{+2.6}_{-3.3}$	$84.5^{+33.8}_{-32.9}$	$-56.4^{+76.4}_{-417.8}$	$41.2^{+29.2}_{-55.0}$	$1.0^{+0.9}_{-1.0}$	$-4.7^{+8.7}_{-13.5}$	$0.6^{+0.3}_{-0.8}$
2020 Jan 28	$694.9^{+26.3}_{-21.7}$	$4.6^{+0.4}_{-0.4}$	$1280.3^{+6.5}_{-6.6}$	$83.2^{+3.6}_{-3.6}$	$1.7^{+0.6}_{-0.6}$	$2.6^{+0.4}_{-0.6}$	$87.8^{+17.3}_{-16.3}$	$18.5^{+3.6}_{-3.8}$	$58.7^{+7.9}_{-9.2}$	$0.8^{+0.3}_{-0.3}$	$-9.2^{+1.1}_{-1.5}$	$0.5^{+0.1}_{-0.1}$
2021 Jan 21	$699.9^{+25.4}_{-26.1}$	$5.9^{+3.3}_{-6.0}$	$1267.1^{+3.4}_{-3.5}$	$79.9^{+9.5}_{-9.2}$	$1.7^{+0.9}_{-1.0}$	$3.5^{+3.4}_{-3.2}$	$85.3^{+53.3}_{-43.4}$	$23.0^{+10.8}_{-37.5}$	$39.1^{+28.3}_{-29.1}$	$0.9^{+0.7}_{-0.7}$	$-3.2^{+9.6}_{-15.5}$	$0.6^{+0.2}_{-0.4}$
2022 Feb 07	$708.0^{+52.0}_{-134.4}$	$5.4^{+1.6}_{-1.1}$	$1264.9^{+2.0}_{-1.7}$	$72.1^{+14.8}_{-14.8}$	$2.0^{+0.6}_{-0.3}$	$6.3^{+1.6}_{-2.1}$	$100.1^{+35.5}_{-33.8}$	$16.9^{+7.9}_{-1.7}$	$54.4^{+8.3}_{-18.6}$	$1.2^{+0.4}_{-0.4}$	$-5.8^{+11.1}_{-12.3}$	$0.5^{+0.1}_{-0.1}$
2023 Jan 15	$604.7^{+52.0}_{-67.2}$	$8.0^{+1.7}_{-2.1}$	$1264.0^{+5.6}_{-6.6}$	$45.4^{+2.4}_{-2.6}$	$1.4^{+2.0}_{-1.6}$	$11.6^{+1.0}_{-0.9}$	$160.8^{+28.0}_{-37.3}$	$12.4^{+1.4}_{-1.4}$	$88.2^{+11.1}_{-4.1}$	$0.2^{+0.3}_{-0.6}$	$-6.9^{+3.6}_{-3.2}$	$0.7^{+0.5}_{-0.5}$

Table A4. Best fit parameters for the two Gaussian model for the central shark fin structure. We show the width σ_b(Å) and σ_{b2}(Å) for each component and the offset in from the central rest Hα wavelength Δ_1(Å) and Δ_2(Å).

Epoch	σ_b(Å)	σ_{b2}(Å)	Δ_1(Å)	Δ_2(Å)
2017 Feb 19	$64.5^{+19.6}_{-23.0}$	$35.7^{+20.5}_{-21.9}$	$-23.7^{+3.7}_{-4.5}$	$-51.9^{+20.2}_{-16.5}$
2017 Feb 27	$43.2^{+4.9}_{-5.5}$	$15.5^{+5.4}_{-6.4}$	$-17.7^{+5.3}_{-6.0}$	$-44.1^{+12.4}_{-13.9}$
2017 Mar 20	$68.4^{+9.6}_{-9.9}$	$25.4^{+13.2}_{-12.3}$	$-22.2^{+1.7}_{-1.7}$	$-53.9^{+10.3}_{-10.3}$
2017 Mar 24	$71.0^{+28.5}_{-42.2}$	$39.5^{+15.3}_{-45.0}$	$-26.4^{+2.8}_{-2.3}$	$-45.6^{+25.1}_{-56.2}$
2017 Apr 04	$63.1^{+20.8}_{-17.7}$	$33.3^{+7.7}_{-8.8}$	$-20.9^{+1.6}_{-1.7}$	$-56.4^{+8.8}_{-16.4}$
2017 Apr 23	$79.9^{+57.3}_{-62.4}$	$27.5^{+5.5}_{-7.1}$	$-19.7^{+3.6}_{-3.4}$	$-38.4^{+22.7}_{-13.5}$
2017 June 29	$62.4^{+28.1}_{-25.4}$	$27.5^{+5.3}_{-4.8}$	$-17.3^{+2.3}_{-2.0}$	$-28.1^{+4.2}_{-4.4}$
2017 Nov 26	$54.4^{+29.6}_{-32.3}$	$38.3^{+19.8}_{-33.6}$	$-23.4^{+5.2}_{-8.0}$	$-42.0^{+21.2}_{-18.8}$
2017 Dec 29	$78.5^{+24.2}_{-26.1}$	$52.1^{+23.2}_{-23.9}$	$-20.3^{+5.3}_{-5.1}$	$-44.1^{+20.4}_{-16.9}$
2018 Jan 05	$56.5^{+32.8}_{-28.9}$	$28.8^{+7.1}_{-13.0}$	$-16.8^{+10.9}_{-7.0}$	$-36.1^{+19.8}_{-10.0}$
2018 Mar 17	$60.8^{+61.5}_{-37.9}$	$26.3^{+71.5}_{-2.7}$	$-18.7^{+21.7}_{-13.0}$	$-26.6^{+58.6}_{-6.7}$
2018 May 15	$126.3^{+25.6}_{-17.7}$	$8.7^{+2.5}_{-2.5}$	$-28.7^{+3.5}_{-2.5}$	$-13.1^{+1.5}_{-2.3}$
2019 Jan 26	$79.9^{+24.6}_{-31.1}$	$39.2^{+9.9}_{-17.5}$	$-20.8^{+9.0}_{-7.6}$	$-51.2^{+16.7}_{-19.3}$
2020 Jan 28	$56.6^{+3.5}_{-3.5}$	$38.5^{+1.9}_{-1.5}$	$-16.0^{+0.9}_{-0.8}$	$-40.9^{+2.5}_{-2.3}$
2021 Jan 21	$70.8^{+27.2}_{-28.6}$	$32.0^{+12.3}_{-13.9}$	$-19.5^{+3.0}_{-2.2}$	$-42.0^{+29.2}_{-16.3}$
2022 Feb 07	$102.6^{+88.6}_{-90.2}$	$22.9^{+1.7}_{-1.8}$	$-34.6^{+17.1}_{-42.2}$	$-21.5^{+1.0}_{-1.4}$
2023 Jan 15	$169.4^{+15.5}_{-14.5}$	$3.2^{+3.3}_{-2.6}$	$-18.2^{+1.4}_{-1.6}$	$-51.0^{+2.9}_{-1.7}$

Table A5. Best-fit parameters for the narrow emission line flux ratios based on modelling of the high-S/N 2020 January 28 spectrum.

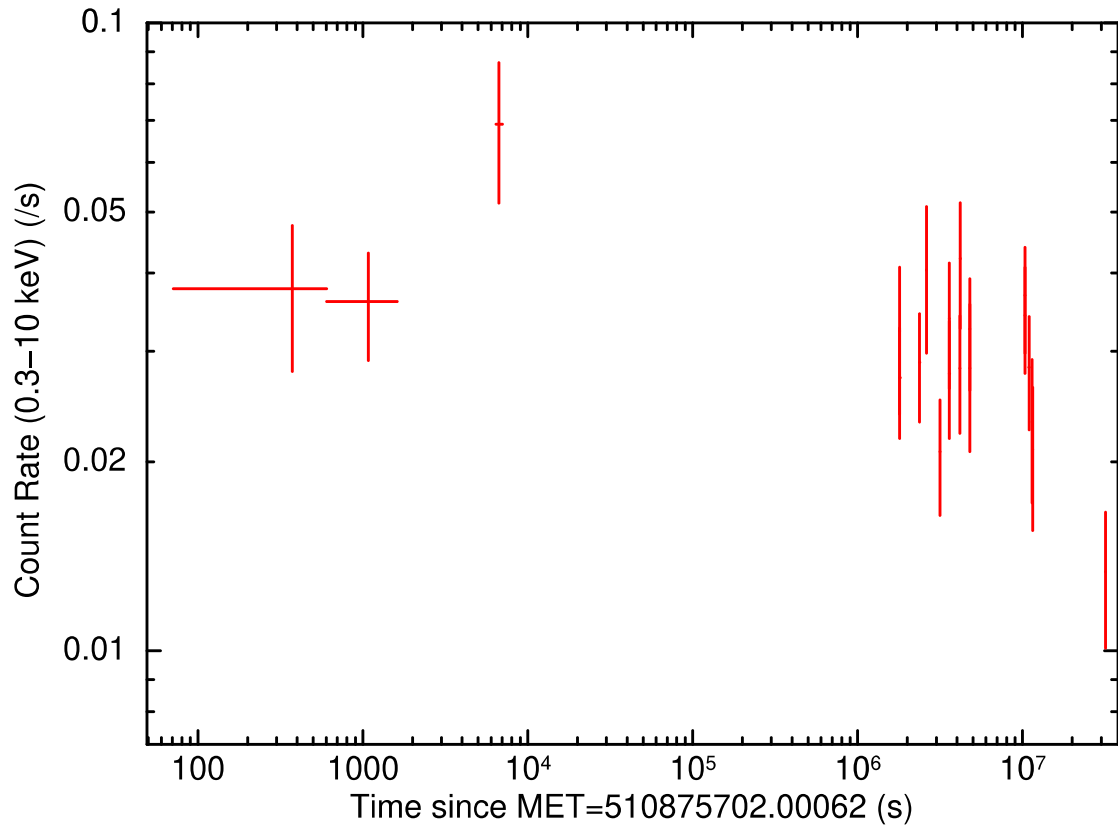| Line ratio	Best fit value	3σ uncertainty
$\log_{10}([\text{N II}]/\text{H}\alpha)$	-1.32	0.11
$\log_{10}([\text{S II}]/\text{H}\alpha)$	-9.90	0.06
$\log_{10}([\text{O I}]/\text{H}\alpha)$	-1.14	0.01
$\log_{10}([\text{O III}]/\text{H}\beta)$	-1.20	0.07

Figure A1. *Swift*/XRT light curve for AT2017bcc, also shown in Table A1.
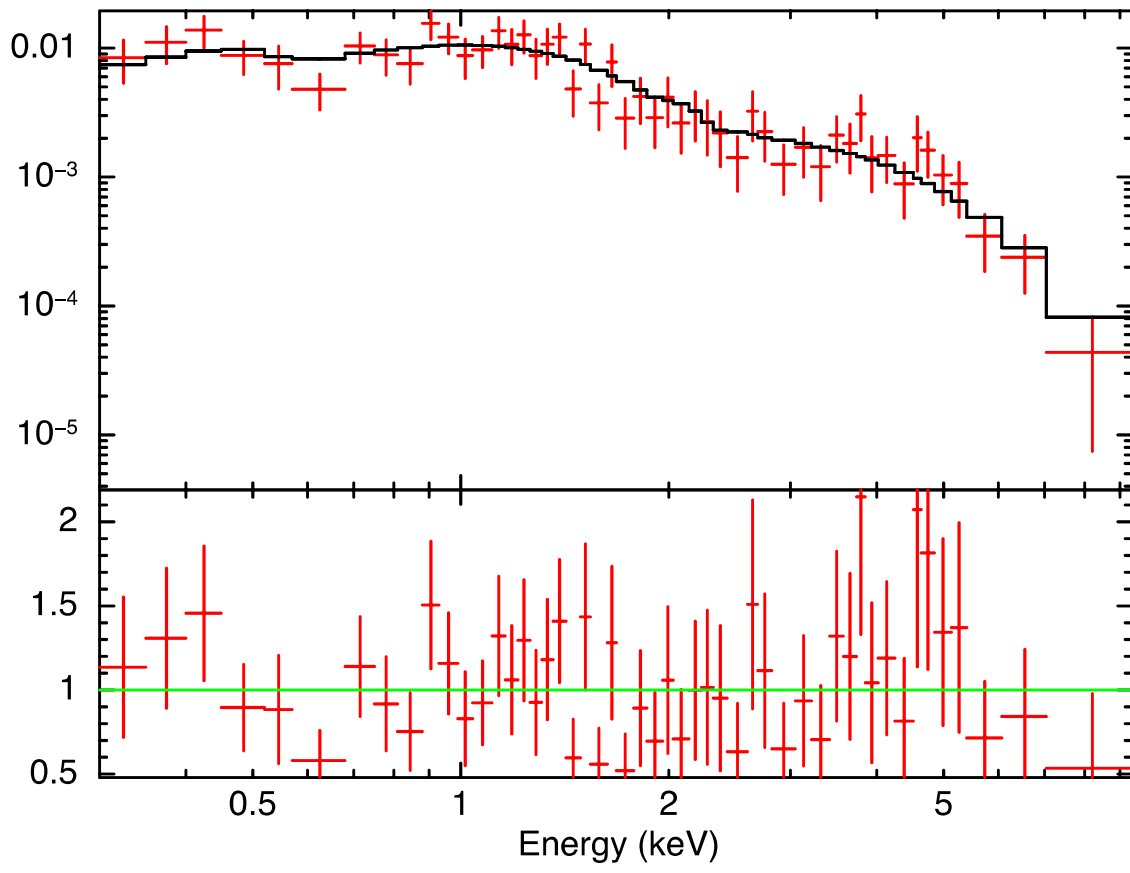
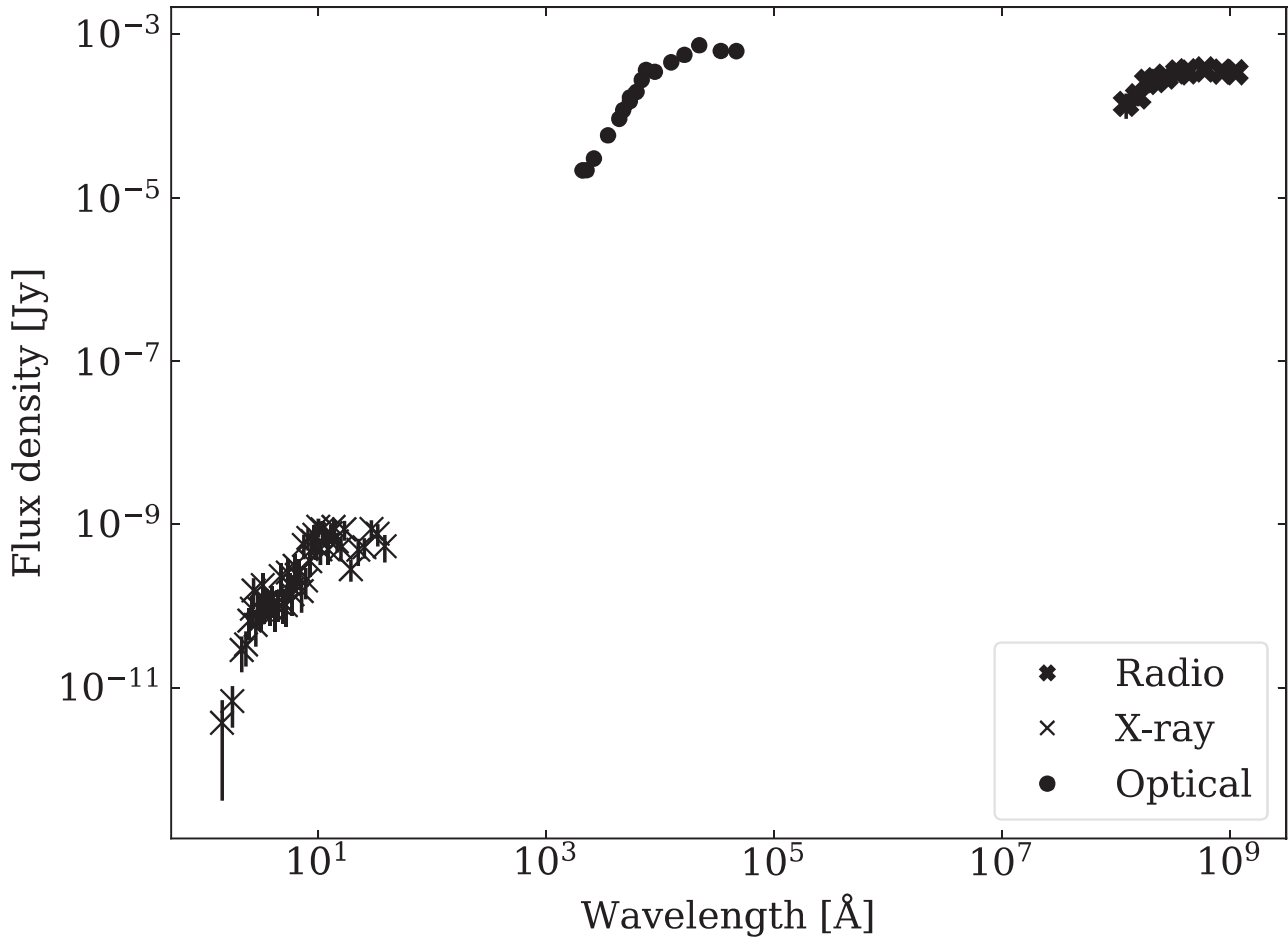**Figure A2.** *Swift*/XRT PC spectrum of AT2017bcc.

Figure A3. Spectral energy distribution across all observed wavelengths of AT2017bcc. The optical fluxes included are from the 2017–05 epoch shown in Fig. 6. The X-ray and radio observations are described in subsections 3.2 and 3.3, respectively.
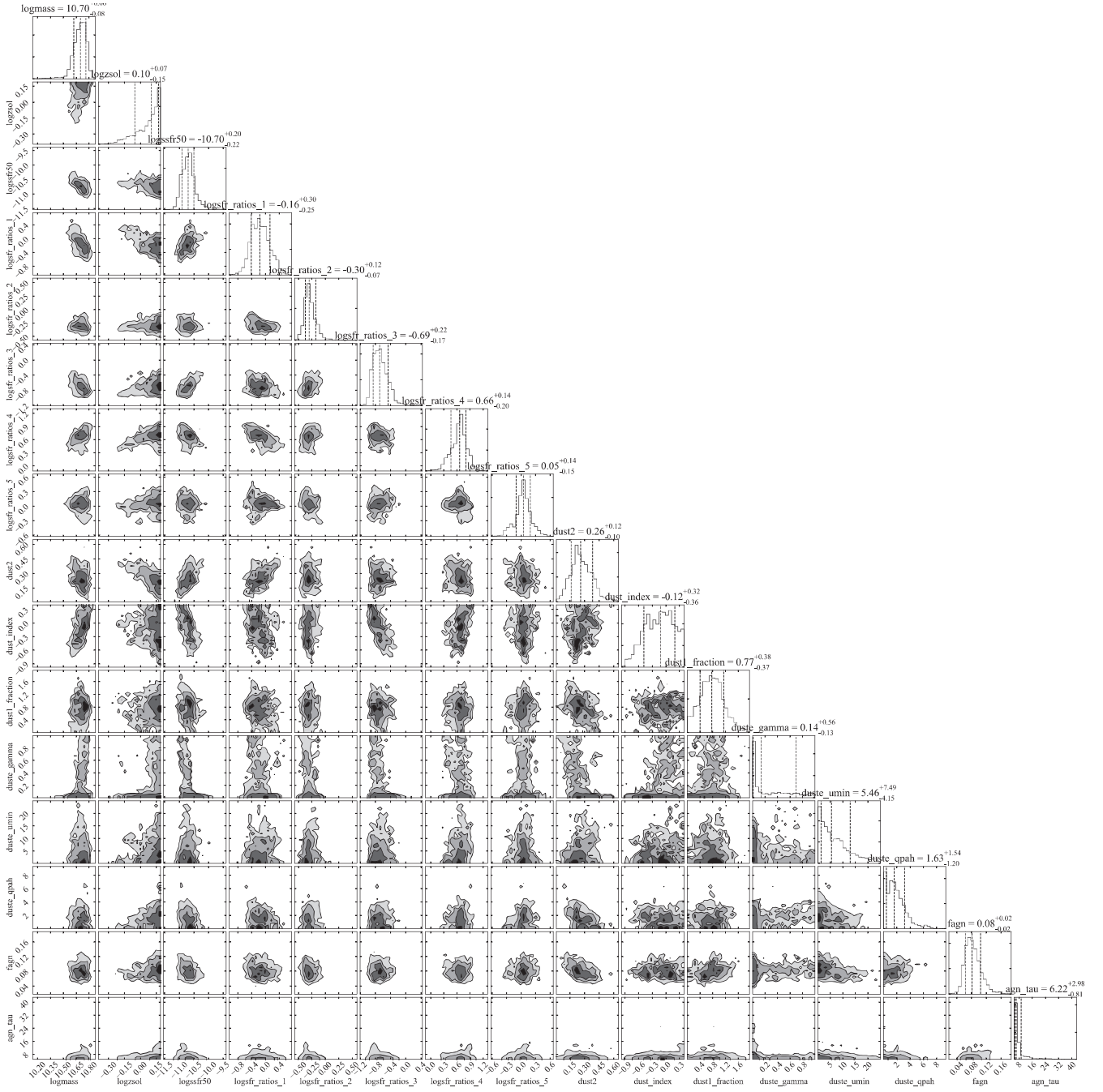
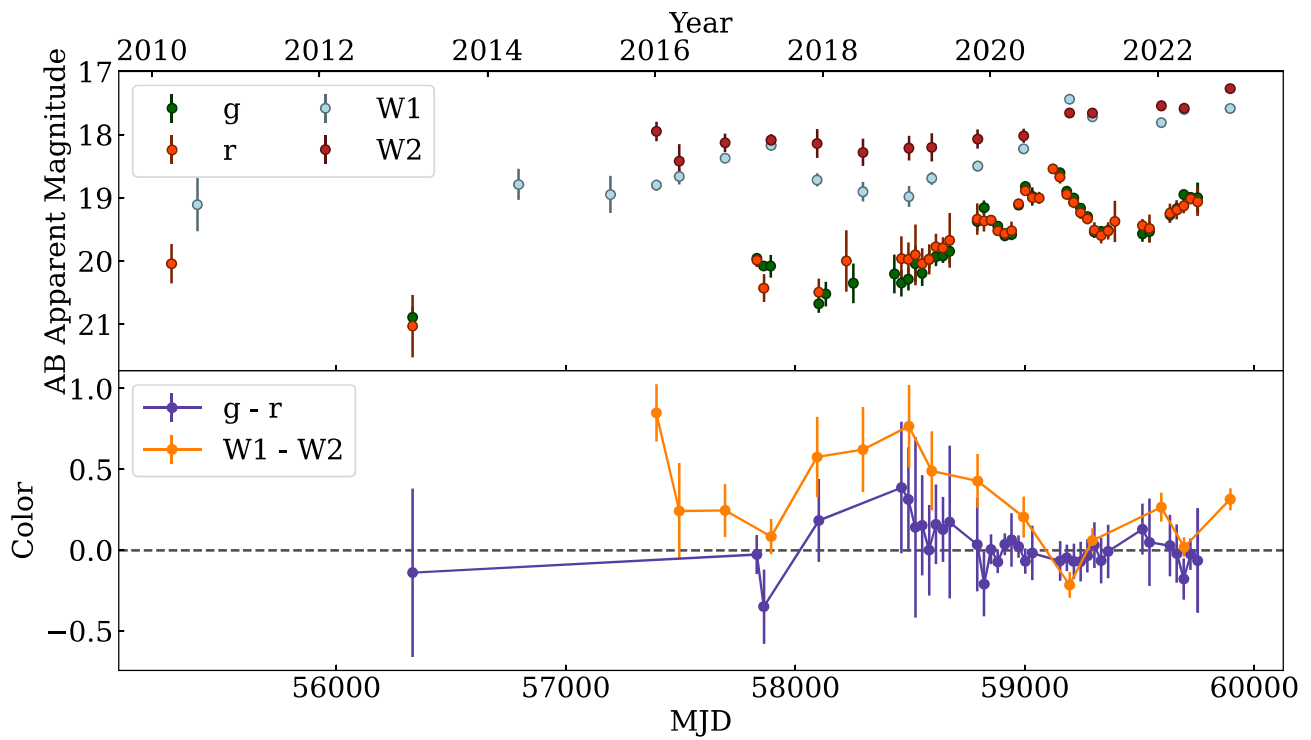**Figure A4.** Corner plot showing results of fitting to host photometry of AT2017bcc using PROSPECTOR.

Figure A5. Host-subtracted light curve of AT2017bcc, with the optical and infrared colour evolution plotted below. Each point is the result of binning fluxes to a monthly cadence before converting to magnitudes and calculating colours. All magnitudes are corrected for galactic extinction and host-subtracted using inferred host fluxes from fits to archival SDSS, 2MASS, and *WISE* photometry, described in Section 4. The optical colours are largely consistent with zero, and are too noisy to show evolution. There may be some evolution in the mid-infrared.
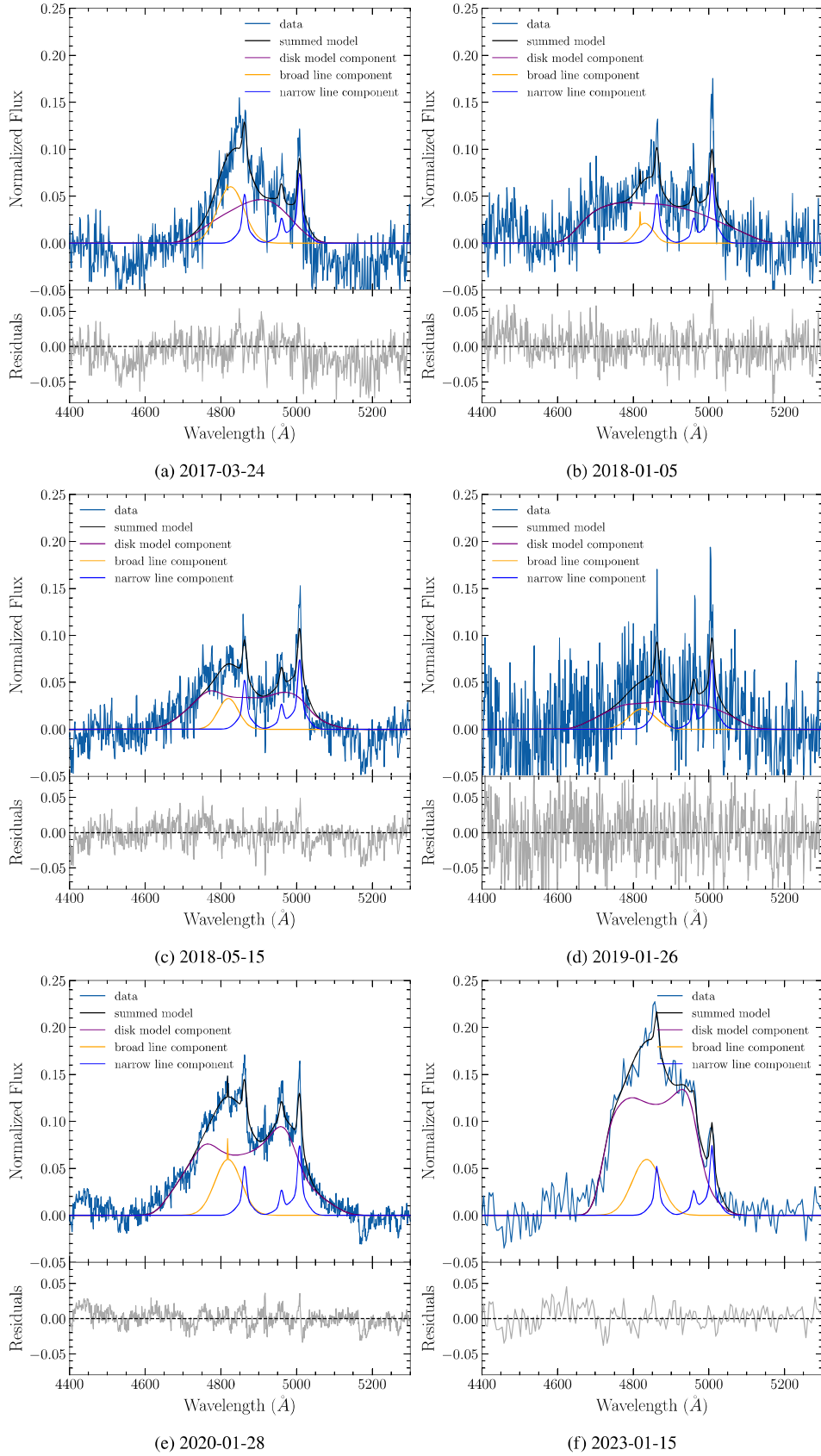
Figure A6. Examples of the best fit Hβ disc and broad line models for 6 different spectral epochs of AT2017bcc corresponding to the fits shown in Fig. 11.
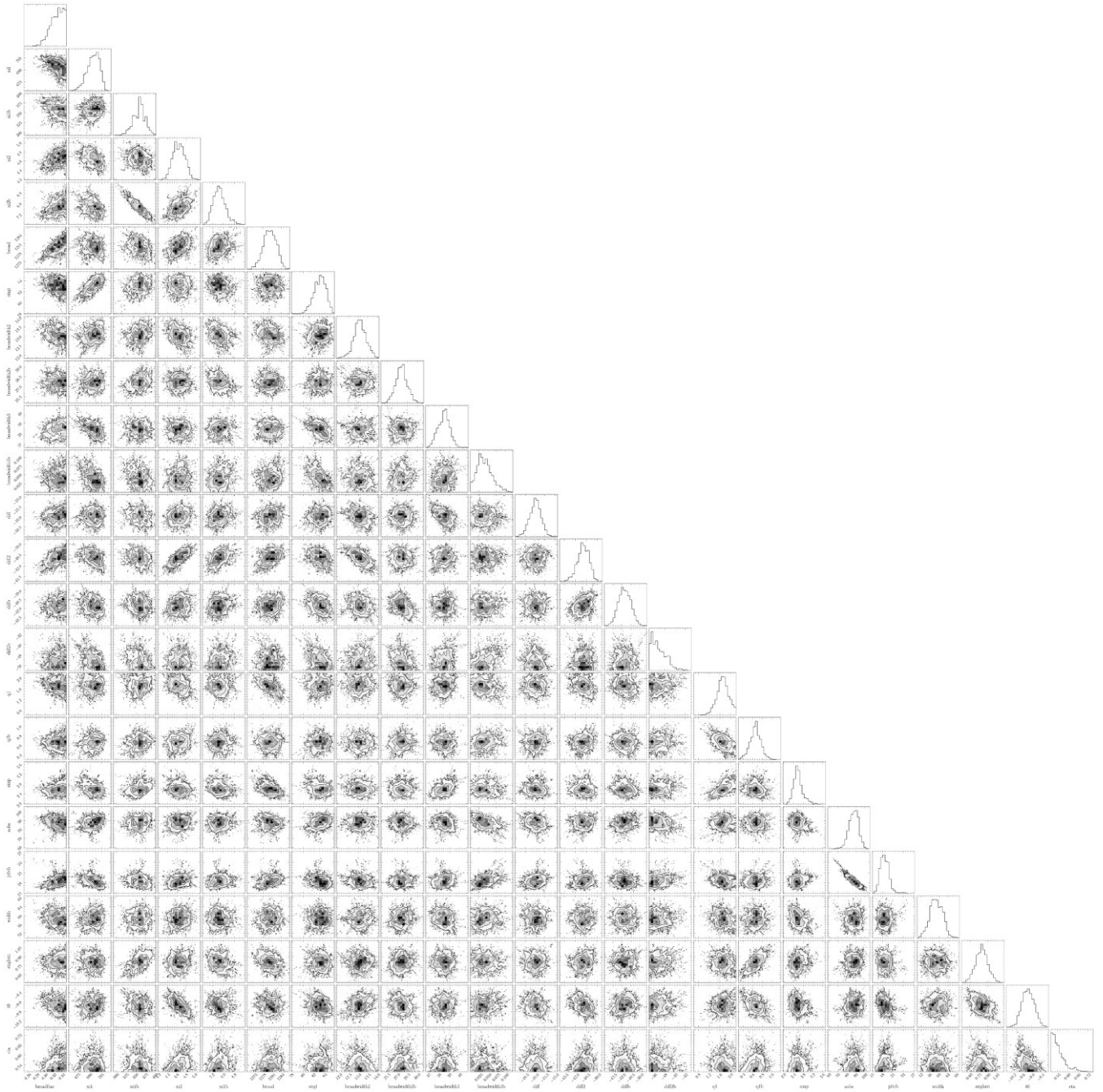
Figure A7. Corner plot for the parameters fit to the 2020 January 28 spectrum describing the disc and outflow components. From left to right we show the following parameters: the ratio of the amplitudes of the H β disc profile and the H α disc profile, the inner radius of the H α emitting region of the disc ξ_1, the inner radius of the H β emitting region of the disc ξ_{1b}, the outer radius of the H α emitting region of the disc ξ_2, the outer radius of the H α emitting region of the disc ξ_{2b}, local turbulent broadening σ, disc inclination angle i, the widths of the two shark fin Gaussian components σ_{b1} and σ_{b2} and their rest wavelength offset from the narrow H α or H β line central wavelengths Δ and Δ_b, the emissivity power-law indices for the H α emitting region and H β emitting regions q and q_b, the spiral arm amplitude A_s, orientation angle ϕ, pitch angle ψ and width w, and the wind opening angle θ, optical depth τ, and the optical depth normalization t_0.
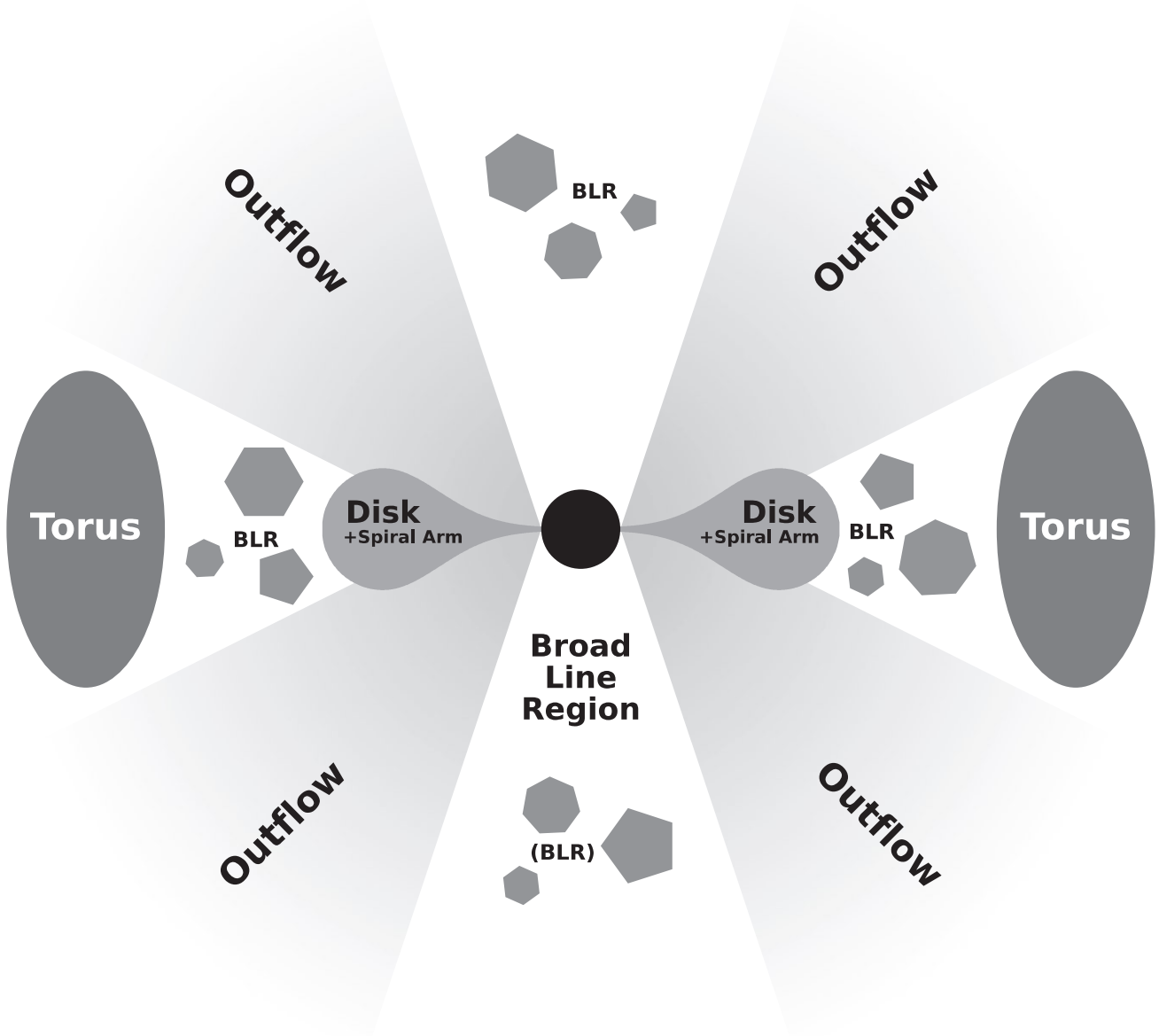
Figure A8. Cross-section diagram of the proposed emitting regions of AT2017bcc described in subsection 6.2. The accretion disc with a spiral arm is shown around the central SMBH, and accounts for the double-peaked component of the emission profile. The double-Gaussian component is comprised of the broad line region (central Gaussian) and the outflow (blueshifted Gaussian). The narrow line emitting regions are expected to exist ∼100 light years from the galactic centre, so are not shown here. Finally, the IR emission likely arises from a dusty torus surrounding the central SMBH, as it reprocesses emission from the AGN.

[1] *School of Physics and Astronomy, University of Birmingham, Edgbaston B15 2TT, UK*

[2] *Institute for Gravitational Wave Astronomy, University of Birmingham, Edgbaston B15 2TT, UK*

[3] *Astrophysics Research Centre, School of Mathematics and Physics, Queen's University Belfast, Belfast BT7 1NN, UK*

[4] *, Department of Astrophysical Sciences, Princeton University, Princeton, NJ 08544, USA*

[5] *Center for Interdisciplinary Exploration and Research in Astrophysics (CIERA), Northwestern University, 1800 Sherman Avenue 8th Floor, Evanston, IL 60201, USA*

[6] *Department of Astronomy, University of California, Berkeley, CA 94720–3411, USA*

[7] *School of Physics, O'Brien Centre for Science North, University College Dublin, Belfield, Dublin 4, D04 P7W1, Ireland*

[8] *Space Telescope Science Institute, 3700 San Martin Drive, Baltimore, MD 21218, USA*

[9] *Department of Physics and Astronomy, University of Turku, FI-20500 Turku, Finland*

[10] *School of Sciences, European University Cyprus, Diogenes Street, Engomi, 1516, Nicosia, Cyprus*

[11] *Department of Physics and Astronomy, Vanderbilt University, Nashville, TN 37235, USA*

[12] *Department of Astronomy/Steward Observatory, 933 North Cherry Avenue, Rm. N204, Tucson, AZ 85721–0065, USA*

[13] *Astronomical Observatory, University of Warsaw, Al. Ujazdowskie 4, PL-00–478 Warszawa, Poland*

[14] *Institute for Astronomy, University of Edinburgh, Royal Observatory, Blackford Hill, Edinburgh EH9 3HJ, UK*

[15] *Cosmic Dawn Center (DAWN), 2800 Kgs. Lyngby, Denmark*

[16] *Niels Bohr Institute, University of Copenhagen, Jagtvej 128, DK-2200 Copenhagen N, Denmark*

[17] *European Southern Observatory, Alonso de Córdova 3107, Casilla 19, Santiago, Chile*

[18] *Millennium Institute of Astrophysics MAS, Nuncio Monsenor Sotero Sanz 100, Off. 104, Providencia, Santiago, Chile*

[19] *INAF-Osservatorio Astronomico di Padova, Vicolo dell'Osservatorio 5, I-35122 Padova, Italy*

[20] *Center for Astrophysics, Harvard & Smithsonian, 60 Garden Street, Cambridge, MA 02138–1516, USA*

[21] *Institute for Astronomy, University of Hawai'i, 2680 Woodlawn Drive, Honolulu, HI 96822, USA*

[22] *Technische Universität München, TUM School of Natural Sciences, Physik-Department, James-Franck-Straße 1, D-85748 Garching, Germany*

[23] *Institut d'Estudis Espacials de Catalunya (IEEC), Gran Capità, 2–4, Edifici Nexus, Desp. 201, E-08034 Barcelona, Spain*

[24] *Institute of Space Sciences (ICE, CSIC), Campus UAB, Carrer de Can Magrans, s/n, E-08193 Barcelona, Spain*

[25] *Cardiff Hub for Astrophysics Research and Technology, School of Physics & Astronomy, Cardiff University, Queens Buildings, The Parade, Cardiff CF24 3AA, UK*

[26] *Finnish Centre for Astronomy with ESO (FINCA), University of Turku, FI-20014 Turku, Finland*

[27] *Tuorla Observatory, Department of Physics and Astronomy, University of Turku, FI-20014 Turku, Finland*

[28] *DTU Space, National Space Institute, Technical University of Denmark, Elektrovej 327, DK-2800 Kgs. Lyngby, Denmark*

[29] *The School of Physics and Astronomy, Tel Aviv University, Tel Aviv 69978, Israel*

[30] *Department of Physics, University of Oxford, Denys Wilkinson Building, Keble Road, Oxford OX1 3RH, UK*

[31] *Department of Astronomy, University of Illinois at Urbana-Champaign, 1002 W. Green Street, Urbana, IL 61801, USA*

[32] *Sternberg Astronomical Institute, Moscow State University, Universitetskii pr. 13, 119992 Moscow, Russia*

This paper has been typeset from a TEX/LATEX file prepared by the author.